Monthly Notices
of the
ROYAL ASTRONOMICAL SOCIETY

MNRAS **465,** 3558–3580 (2017)
Advance Access publication 2016 November 20

doi:10.1093/mnras/stw2911

The *Herschel*-ATLAS: a sample of 500 μm-selected lensed galaxies over 600 deg^2

M. Negrello,[1⋆] S. Amber,[2] A. Amvrosiadis,[1] Z.-Y. Cai,[3] A. Lapi,[4,5] J. Gonzalez-Nuevo,[6] G. De Zotti,[5,7] C. Furlanetto,[8,9] S. J. Maddox,[1,10] M. Allen,[1] T. Bakx,[1] R. S. Bussmann,[11] A. Cooray,[12] G. Covone,[13] L. Danese,[5] H. Dannerbauer,[14,15] H. Fu,[16] J. Greenslade,[17] M. Gurwell,[18] R. Hopwood,[17] L. V. E. Koopmans,[19] N. Napolitano,[20] H. Nayyeri,[12] A. Omont,[21,22] C. E. Petrillo,[19] D. A. Riechers,[11] S. Serjeant,[2] C. Tortora,[19] E. Valiante,[1] G. Verdoes Kleijn,[19] G. Vernardos,[19] J. L. Wardlow,[23] M. Baes,[24] A. J. Baker,[25] N. Bourne,[10] D. Clements,[17] S. M. Crawford,[26] S. Dye,[8] L. Dunne,[1,10] S. Eales,[1] R. J. Ivison,[10,27] L. Marchetti,[2,26] M. J. Michałowski,[10] M. W. L. Smith,[1] M. Vaccari[28,29] and P. van der Werf[30]

Affiliations are listed at the end of the paper

Accepted 2016 November 7. Received 2016 October 6; in original form 2016 July 20

ABSTRACT

We present a sample of 80 candidate strongly lensed galaxies with flux density above 100 mJy at 500 μm extracted from the *Herschel* Astrophysical Terahertz Large Area Survey, over an area of 600 deg^2. Available imaging and spectroscopic data allow us to confirm the strong lensing in 20 cases and to reject it in one case. For other eight objects, the lensing scenario is strongly supported by the presence of two sources along the same line of sight with distinct photometric redshifts. The remaining objects await more follow-up observations to confirm their nature. The lenses and the background sources have median redshifts $z_{\rm L} = 0.6$ and $z_{\rm S} = 2.5$, respectively, and are observed out to $z_{\rm L} = 1.2$ and $z_{\rm S} = 4.2$. We measure the number counts of candidate lensed galaxies at 500 μm and compare them with theoretical predictions, finding a good agreement for a maximum magnification of the background sources in the range 10–20. These values are consistent with the magnification factors derived from the lens modelling of individual systems. The catalogue presented here provides sub-mm bright targets for follow-up observations aimed at exploiting gravitational lensing, to study with unprecedented details the morphological and dynamical properties of dusty star-forming regions in $z \gtrsim 1.5$ galaxies.

Key words: gravitational lensing: strong – galaxies: evolution – galaxies: high-redshift – submillimetre: galaxies.

1 INTRODUCTION

Wide-area extragalactic surveys performed at sub-millimeter (sub-mm) to millimeter (mm) wavelengths with the *Herschel Space Observatory* (Pilbratt et al. 2010) and the South Pole Telescope (SPT; Carlstrom et al. 2011) have led to the discovery of several dusty star-forming galaxies (DSFGs) at $z \gtrsim 1$ whose luminosity is magnified by a foreground galaxy or a group/cluster of galaxies (Negrello et al. 2010, 2014; Conley et al. 2011; Cox et al. 2011; Bussmann et al. 2012, 2013; Vieira et al. 2013; Wardlow et al. 2013; Calanog et al. 2014; Messias et al. 2014; Dye et al. 2015; Nayyeri et al. 2016; Spilker et al. 2016). The selection of strongly lensed galaxies at these wavelengths is made possible by the (predicted) steep number counts of high-redshift sub-mm galaxies (Blain 1996; Negrello et al. 2007); in fact, almost exclusively, those galaxies whose flux density has been boosted by an event of lensing can be observed above a certain threshold, namely ∼100 mJy at 500 μm (Negrello et al. 2010; Wardlow et al. 2013).

By means of a simple selection in flux density at 500 μm, Negrello et al. (2010) produced the first sample of five strongly lensed galaxies from 16 deg^2 of the sky observed with *Herschel*

⋆ E-mail: NegrelloM@cardiff.ac.uk

during the Science Demonstration Phase (SDP) as part of the *Herschel* Astrophysical Terahertz Large Area Survey[1] (Eales et al. 2010, *H*-ATLAS hereafter). Preliminary source catalogues derived from the full *H*-ATLAS were then used to identify the sub-mm brightest candidate lensed galaxies for follow-up observations with both ground based and space telescopes to measure their redshifts (Frayer et al. 2011; Omont et al. 2011, 2013; Valtchanov et al. 2011; Harris et al. 2012; Lupu et al. 2012; George et al. 2013; Messias et al. 2014) and confirm their nature (Negrello et al. 2010, 2014; Bussmann et al. 2012, 2013; Fu et al. 2012; Calanog et al. 2014). Using the same methodology, i.e. a cut in flux density at 500 μm, Wardlow et al. (2013) have identified 11 lensed galaxies over 95 deg^2 of the *Herschel* Multi-tiered Extragalactic Survey (HerMES; Oliver et al. 2012), while, more recently, Nayyeri et al. (2016) have published a catalogue of 77 candidate lensed galaxies with $F_{500} \geq 100$ mJy extracted from the HerMES Large Mode Survey (HeLMS; Oliver et al. 2012) and the *Herschel* Stripe 82 Survey (HerS; Viero et al. 2014), over an area of 372 deg^2. All together, the extragalactic surveys carried out with *Herschel* are expected to deliver a sample of more than a hundred of sub-mm bright strongly lensed galaxies, which, as argued by Gonzalez-Nuevo et al. (2012), might increase to over a thousand if the selection is based on the steepness of the luminosity function of DSFGs (Lapi et al. 2011) rather than that of the number counts. Similarly, at mm wavelengths, the SPT survey has already discovered several tens of lensed galaxies (e.g. Vieira et al. 2013; Spilker et al. 2016) and other lensing events have been found in the *Planck* all-sky surveys (Cañameras et al. 2015; Planck Collaboration XXVII 2015; Harrington et al. 2016)

Having a large sample of strongly lensed DSFGs is important for several reasons. (i) Thanks to the boosting in luminosity and increase in angular size offered by gravitational lensing, distant galaxies can be studied with unprecedented details down to sub-kpc scales. For sub-mm/mm-selected sources, this means understanding the morphological and dynamical properties of individual giant molecular clouds in a statistically significant sample of dusty galaxies across the peak of the cosmic star formation history of the Universe (e.g. Swinbank et al. 2010; Dye et al. 2015). (ii) The observed lensed morphology is determined by the content and the spatial distribution of the total (baryonic+dark) matter in the foreground galaxy; therefore, by means of high-resolution imaging data at sub-mm/mm wavelengths – as now provided by the Atacama Large Millimeter Array (ALMA) – gravitational lensing allows the detection of low-mass sub-structures in the lenses, whose abundance can be used to test the cold-dark-matter scenario of structure formation on small scales (e.g. Mao & Schneider 1998; Metcalf & Madau 2001; Dalal & Kochanek 2002; Vegetti et al. 2012; Hezaveh et al. 2013, 2016; Inoue et al. 2016); in this respect, it is worth noticing that for sub-mm/mm-selected lensed galaxies, the contamination of the lens – typically a passively evolving elliptical galaxy – to the sub-mm emission of the background galaxy is negligible. Therefore, the modelling of the lensed morphology does not suffer from uncertainties on the lens subtraction, as usually happens in optically selected lensing systems; furthermore, since the sample of lensed galaxies is constructed by exploiting the properties of the background galaxy alone, i.e. its sub-mm flux density, it is less biased against the redshift and the mass of the lens, compared to standard optical/spectroscopic selection techniques, thus allowing us to probe the mass distribution of foreground galaxies out to $z \gtrsim 1$(e.g. Dye et al. 2014). (iii) The statistics of lenses, as well as the distribution and extent of the image separations, depend on the dark-matter and dark-energy content of the Universe; therefore, large samples of gravitational lenses can be used to constrain cosmological parameters (e.g. Grillo, Lombardi & Bertin 2008; Eales 2015).

Here, we present the sample of candidate lensed galaxies with $F_{500} \geq 100$ mJy extracted from the ∼600 deg^2 of the full *H*-ATLAS. The work is organized as follows. The *H*-ATLAS catalogue and available ancillary data sets are presented in Section 2. In Section 3, we describe the selection of the candidate lensed galaxy and discuss the properties of the sample. In Section 4, we derive the number counts of lensed galaxies and compare them with model predictions. Conclusions are summarized in Section 5.

The modelling of the number counts is made assuming a spatially flat cosmological model with present-day matter density in units of the critical density, $\Omega_{0,\,\mathrm{m}} = 0.308$ and Hubble constant $H_0 = 67.7\,\mathrm{km\,s^{-1}\,Mpc^{-1}}$, spectrum of primordial density perturbations with slope $n = 1$ and normalization on a scale of $8\,h^{-1}$ Mpc $\sigma_8 = 0.81$ (Planck Collaboration XIII 2016).

2 DATA SETS

H-ATLAS is the widest-area extragalactic survey undertaken with *Herschel*, imaging around 600 deg^2 of the sky in five far-infrared (far-IR) to sub-mm bands, 100, 160, 250, 350 and 500 μm, using the PACS (Poglitsch et al. 2010) and SPIRE (Griffin et al. 2010) instruments, in parallel mode. *H*-ATLAS covers five fields: three fields on the celestial equator, each about 54 deg^2 in size and approximatively located at right ascension RA = 9^h, 12^h and 15^h, a large (∼170 deg^2) field close to the North Galactic Pole (NGP) and an even larger field (∼270 deg^2) near the South Galactic Pole (SGP).

The fields were selected to minimize bright continuum emission from dust in the Galaxy, as traced at 100 μm by the *Infrared Astronomical Satellite*, and to benefit from existing data at other wavelengths, particularly spectroscopic optical data provided by other major surveys of the nearby Universe, e.g. the Galaxy And Mass Assembly (GAMA) survey[2] (Driver et al. 2009, 2016), the Sloan Digital Sky Survey (SDSS; Abazajian et al. 2009), the 2-Degree-Field Galaxy Redshift Survey (Colless et al. 2001) and the Kilo-Degree Survey (KiDS; de Jong et al. 2015). Apart from optical imaging and spectroscopy, the fields have imaging data at near-IR wavelengths from the UK Infrared Deep Sky Survey Large Area Survey (UKIDSS-LAS; Lawrence et al. 2007) and the VISTA Kilo-Degree Infrared Galaxy Survey (VIKING; Edge et al. 2013). Radio-imaging data in the fields are provided by the Faint Images of the Radio Sky at Twenty-cm survey and the NRAO Very Large Array Sky Survey.

Candidate lensed galaxies were selected from the *Herschel*/SPIRE (Griffin et al. 2010) catalogue of the *H*-ATLAS Data Release 1 and 2 (Valiante et al. 2016). These catalogues are created in two stages. First, the Multiband Algorithm for source Detection and eXtraction (MADX; Maddox et al., in preparation) is used to identify the 2.5σ peaks in the 250 μm maps and to measure the flux densities at the position of those peaks in all the SPIRE bands. The maps used for the flux measurements have been filtered with a matched-filter technique (Chapin et al. 2011) to minimize instrumental and confusion noise. Secondly, only sources with

[1] www.h-atlas.org

[2] The *H*-ATLAS equatorial fields are also referred to as the *H*-ATLAS/GAMA fields

signal-to-noise ratio ≥4 in at least one of the three SPIRE bands are kept in the final catalogue. The 4σ detection limit at 250 μm for a point source ranges from 24 mJy in the deepest regions of the maps (where tiles overlap) to 29 mJy in the non-overlapping regions. For more details about the source extraction procedure and the flux-density measurements, we refer the reader to Valiante et al. (2016). The catalogue and the maps will be made available at the *H*-ATLAS website: www.h-atlas.org.

Flux-density measurements for extended galaxies are currently only available for sources detected in the *H*-ATLAS equatorial fields. Therefore, in the present analysis, we only use point-source flux densities. This is not an issue for lensed galaxies, as they do appear as point sources in the SPIRE maps. Extended galaxies are treated as contaminants to be removed from the final sample and they are identified by means of available optical imaging data; therefore, their precise flux density at sub-mm wavelengths is not a concern. We warn the reader against using the number of local galaxies with $F_{500} \geq 100$ mJy derived here for comparison with theoretical models, as such number is significantly underestimating the true density of local galaxies that have 500 μm flux density above the adopted threshold.

The redshift of several lensed galaxies discovered in *H*-ATLAS has been constrained through the detection of rest-frame far-IR/sub-mm emission lines from carbon monoxide (CO), water vapour (H_2O), ionized carbon (C II) and doubly ionized oxygen ([O III]), using Z-spec (Lupu et al. 2012), GBT/Zspectrometer (Frayer et al. 2011; Harris et al. 2012), PdBI (Negrello et al. 2010; Omont et al. 2011, 2013; Yang et al. 2016, George et al., in preparation), CARMA (Riechers et al., in preparation) and the *Herschel*/SPIRE Fourier Transform Spectrometer (Valtchanov et al. 2011; George et al. 2013).

Optical spectra of the lenses in confirmed *H*-ATLAS-selected lensing systems were taken with the William Herschel Telescope, the Apache Point Observatory 3.5 metre telescope (Negrello et al. 2010), the New-Technology Telescope (NTT; Amber 2015), the Gemini-South telescope (Bussmann et al. 2013) and the Anglo Australian Telescope as part of GAMA. A project is ongoing to get optical spectra with the South African Large Telescope (SALT; Serjeant 2016, Marchetti et al., in preparation).

Near-IR follow-up observations with the *Hubble Space Telescope* (*HST*) and the *Keck* telescope in adaptive optics (AO) are available for tens of candidate lensed galaxies in the *H*-ATLAS fields (Fu et al. 2012; Bussmann et al. 2013; Calanog et al. 2014; Negrello et al. 2014). Some of these sources have also been observed with the Sub-millimeter Array (SMA) at ∼0.5 arcsec resolution at 880 μm (Negrello et al. 2010; Bussmann et al. 2012, 2013), while six of them have been recently imaged in band 7 with the ALMA with better resolution and sensitivity (PI: Eales). A lens modelling of the ALMA data will be presented in future papers (Dye et al., in preparation; Negrello et al., in preparation).

3 CANDIDATE LENSED GALAXIES

We describe below the procedure adopted to identify candidate lensed galaxies in the *H*-ATLAS and discuss the main properties of the sample.

3.1 Selection

According to model predictions (Blain 1996; Perrotta et al. 2002, 2003; Lapi et al. 2006, 2011; Negrello et al. 2007, 2010), the number counts of unlensed DSFGs are expected to drop abruptly at 500 μm flux densities of ≃100 mJy, as an effect of the intrinsically steep luminosity function and high redshift ($z \gtrsim 1.5$) of these sources. Therefore, we start by selecting all the sources with $F_{500} \geq 100$ mJy. They are 325 in total. A fraction of these sources are either low-redshift ($z \lesssim 0.1$) spiral galaxies or flat spectrum radio sources (e.g. Negrello et al. 2007). Both of these classes of objects are considered as 'contaminants' for the purpose of this paper, and therefore need to be identified and removed. We used the interactive software sky atlas ALADIN (Bonnarel et al. 2000) to inspect available optical, IR and radio imaging data and to query the NASA/IPAC Extragalactic Database[3] (NED) around the position of each source.

We identified 11 blazars, according to their intense radio emission ($F_{1.4\mathrm{GHz}} > 100$ mJy) and the rising/flat spectral energy distribution (SED) from sub-mm to radio wavelengths. They are listed in Table 1. Their number density is consistent with theoretical expectations (e.g. Tucci et al. 2011). Two of them were previously reported by Lopez-Caniego et al. (2013) who searched for blazars in 135 deg^2 of the *H*-ATLAS equatorial fields.

231 spiral-like galaxies with an angular size exceeding several arcseconds in optical images were categorized as local galaxies. All were confirmed as local galaxies via available spectroscopic redshift. Their redshift distribution is shown in Fig. 1. Two galaxies have $z > 0.1$: HATLASJ090734.8+012504 ($z = 0.102\,315$) and HATLASJ120226.7−012915 ($z = 0.150\,694$), which would place them in the right redshift range for acting as gravitational lenses. However, in these cases, we can exclude that the sub-mm emission, as measured by *Herschel*, is coming from a more distant background galaxy that has been gravitationally lensed. In fact, in both cases, the *Herschel*/SPIRE colours are consistent with the measured spectroscopic redshift: $F_{250}/F_{350} = 2.4$ and $F_{350}/F_{500} = 3.1$ for HATLASJ090734.8+012504, and similarly $F_{250}/F_{350} = 2.4$ and $F_{350}/F_{500} = 2.7$ for HATLASJ120226.7−012915 (see also Section 3.3 and the related Fig. 4).

After this process, we are left with 83 objects, three of which are found to be dusty stars: HATLASJ132301.6+341649 in the NGP field and HATLASJ225739.6-293730 and HATLASJ012657.9-323234 in the SGP field. They are listed in Table 2. While the ones in the SGP field are well-known stars with IR emission, the one in the NGP was identified as such based on its star-like classification in SDSS, its point-like appearance in available *HST*/Wide Field Camera 3 (WFC3) imaging data and its measured non-null proper motion (23.3 ± 4.5 mas yr^{-1}) in the United States Naval Observatory catalogue. The remaining 80 sources are retained as *candidate lensed galaxies*. Table 3 summarizes the result of the classification. It is worth mentioning that our selection method picked up an extra candidate lensed galaxy, HATLASJ120735.6+005400, in the 12 $^{\mathrm{h}}$ equatorial field, which, however, is not included in the current sample. Indeed, this source turned out to be an asteroid (3466 Ritina) and as such it was removed from the publicly released *H*-ATLAS catalogue (Valiante et al. 2016).

The 80 candidate lensed galaxies are listed in Table 4 together with their *Herschel*/SPIRE photometry and other additional information. Fig. 2 shows their distribution within the five *H*-ATLAS fields. The 16 deg^2 SDP field, marked by the white frame in the figure, was a lucky choice in terms of detecting lensed galaxies: it contains five confirmed lensed sources with $F_{500} \geq 100$ mJy (Negrello et al. 2010). On average, within a similar area, we would have expected $80/602 \times 16 \simeq 2$ lensed galaxies with 500 μm flux density above the 100 mJy threshold.

[3] http://ned.ipac.caltech.edu/

Table 1. Blazars with $F_{500} \geq 100$ mJy identified in the *H*-ATLAS fields. *Herschel*/SPIRE flux densities are provided together with 1.4 GHz flux densities and spectroscopic redshifts (from NED).

H-ATLAS IAU name	NED name	F_{250} (mJy)	F_{350} (mJy)	F_{500} (mJy)	$F_{1.4\mathrm{GHz}}$ (mJy)	z_{spec}
HATLASJ090910.1+012134[a, b]	[HB89] 0906+015	256.5 ± 6.4	327.1 ± 7.4	375.3 ± 8.1	760 ± 23	1.024 905
HATLASJ121758.7−002946	PKS 1215−002	122.7 ± 7.4	152.3 ± 8.1	177.5 ± 8.4	452 ± 16	0.418 406
HATLASJ141004.7+020306[b]	[HB89] 1407+022	119.4 ± 7.3	151.0 ± 8.4	176.0 ± 8.7	334 ± 10	1.253 000
HATLASJ131028.7+322043	[HB89] 1308+326	259.1 ± 6.7	363.1 ± 7.7	452.2 ± 8.1	1687 ± 51	0.998 007
HATLASJ125757.3+322930	7C 1255+3245	143.7 ± 7.3	188.4 ± 8.2	214.9 ± 8.6	653 ± 20	0.805 949
HATLASJ133307.3+272518	87GB 133047.7+274044	89.3 ± 7.4	104.6 ± 8.1	117.1 ± 8.3	218 ± 7	2.126 000
HATLASJ131736.4+342518	[HB89] 1315+346	77.1 ± 7.2	99.5 ± 8.0	112.0 ± 8.7	529 ± 16	1.055 411
HATLASJ014503.3−273332	[HB89] 0142−278	131.5 ± 5.7	179.1 ± 6.3	233.5 ± 7.2	923 ± 28	1.155 000
HATLASJ224838.6−323550	[HB89] 2245−328	119.2 ± 5.5	152.8 ± 5.8	194.8 ± 6.7	708 ± 21	2.268 000
HATLASJ014309.9−320056	PKS 0140−322	96.0 ± 5.3	119.5 ± 5.9	122.4 ± 7.2	76 ± 2	0.375 100
HATLASJ235347.4−303745	PKS 2351−309	77.1 ± 5.1	96.6 ± 5.8	103.1 ± 7.0	398 ± 14	–

Notes. [a]Also reported in Gonzalez-Nuevo et al. (2010). [b]Also reported in Lopez-Caniego et al. (2013).

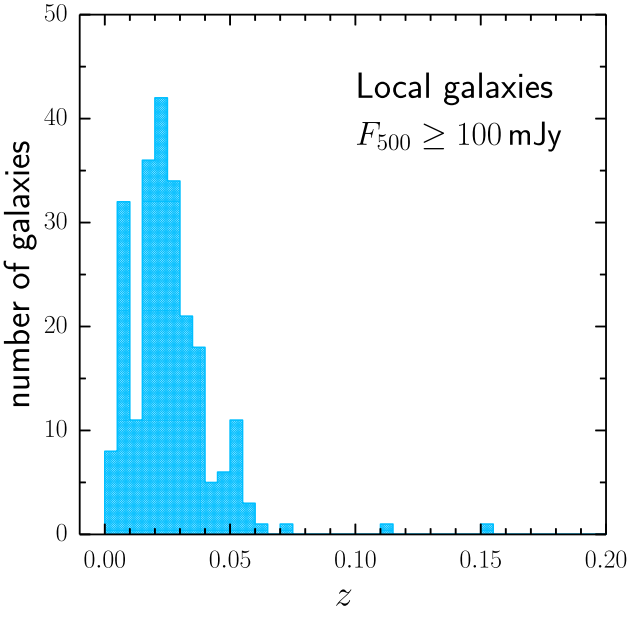

Figure 1. Redshift distribution of local galaxies with $F_{500} \geq 100$ mJy (blue) identified in the *H*-ATLAS equatorial fields. The sources at $z > 0.1$ are HATLASJ090734.8+012504 ($z = 0.102\,315$) and HATLASJ120226.7−012915 ($z = 0.150\,694$).

3.2 Confirmed lensed and unlensed galaxies

The sample includes 20 sources that have already been confirmed to be strongly lensed via the detection of multiple images or arcs in the near-IR with *HST* and *Keck*/AO or, in the sub-mm, with the SMA, and via the measurement of two distinct redshifts along the same line of sight. They are shown in Fig. 3. None of them lie in the SGP field because the *Herschel* data for that field were the latest to be delivered and processed, while most of the follow-up efforts have been focused on the other *H*-ATLAS fields. The confirmed lensed galaxies comprise 80 per cent of the sub-sample of candidate lensed galaxies with $F_{500} \geq 150$ mJy identified in the equatorial and NGP fields (i.e. 17 out of 21). Among them are the first five lensed galaxies discovered by the *H*-ATLAS (Negrello et al. 2010). The others are from Bussmann et al. (2012, 2013), Fu et al. (2012), Messias et al. (2014) and Calanog et al. (2014). While most of them are galaxy-scale lenses, the sample includes also two group-lenses (HATLASJ114637.9-001132, HATLASJ133542.9+300401) as well as two cluster-lenses (HATLASJ141351.9-000026, HATLASJ132427.0+284449) producing giant (∼10 arcsec in near-IR images) arcs.

The lenses in the sample exhibit a wide range of redshifts, from $z_{\mathrm{L}} = 0.22$ up to 1.22, with a median redshift $z_{\mathrm{L}} = 0.6$. This is a consequence of our selection technique, which is based exclusively on the observed properties of the background source, i.e. its flux density. No prior information on the lens properties is introduced during the lensed galaxy search. This means that samples of sub-mm-selected lenses can allow us to study of the evolution of the mass density profile of galaxies out to high redshift ($z > 1$) and over a wide range of galaxy masses (e.g. Dye et al. 2014).

Table 3. Number of sources with $F_{500} \geq 100$ mJy classified as candidate lensed galaxies, local (late-type) galaxies, blazars and dusty stars in the *H*-ATLAS fields.

	Candidate lensed galaxies	Local galaxies	Blazars	Dusty stars
9^{h} field	9	10	1	0
12^{h} field	12	18	1	0
15^{h} field	5	32	1	0
NGP field	24	84	4	1
SGP field	30	87	4	2
Total	80	231	11	3

Table 2. Dusty stars with $F_{500} \geq 100$ mJy identified in the *H*-ATLAS fields. The *Herschel*/SPIRE flux densities are provided.

H-ATLAS IAU name	NED name	F_{250} (mJy)	F_{350} (mJy)	F_{500} (mJy)
HATLASJ132301.6+341649	SDSS J132301.74+341647.8	124.2 ± 7.3	144.6 ± 8.2	137.0 ± 8.7
HATLASJ225739.6−293730	αPsA (Fomalhaut)	825.2 ± 5.7	433.0 ± 6.1	292.1 ± 7.3
HATLASJ012657.9−323234	R Sclulptoris	795.6 ± 5.5	541.7 ± 6.0	242.4 ± 7.1

Table 4. List of candidate lensed galaxies with $F_{500} \geq 100$ mJy extracted from the ∼600 deg^2 of the *H*-ATLAS fields. For each source the following information is provided: *Herschel*/SPIRE flux densities; reliability of association with any SDSS source within 5 arcsec from the SPIRE position and with $r < 22.4$ (Bourne et al. 2016; Furlanetto et al. 2016); distance of the SDSS source from the SPIRE detection and its AB *r*-band magnitude; redshift of the SDSS association and of the SPIRE source (when no spectroscopic measurement is available, the photometric redshift is provided instead, in italic style); lensing rank: A = confirmed to be lensed, B = likely to be lensed, C = unclear, D = not (strongly) lensed; magnification factor derived from the modelling of high-resolution sub-mm/mm imaging data.

H-ATLAS IAU name	F_{250} (mJy)	F_{350} (mJy)	F_{500} (mJy)	reliab. SDSS-ID	sep(arcsec) SDSS-ID	*r*-mag SDSS-ID	$z_{\rm opt}$	$z_{\rm sub-mm}$	Lensing rank	$\mu_{\rm sub-mm}$
GAMA-9$^{\rm h}$ field (53.4 deg^2)										
HATLASJ083051.0+013225(B13)	248.5 ± 7.5	305.3 ± 8.1	269.1 ± 8.7	0.958	1.81	21.6	0.626+1.002	3.634[a]	A	6.9 ± 0.6
HATLASJ085358.9+015537(B13)	396.4 ± 7.6	367.9 ± 8.2	228.2 ± 8.9	–	–	–		2.0925[b]	A	15.3 ± 3.5
HATLASJ091043.0−000322(SDP.11)	420.8 ± 6.5	370.5 ± 7.4	221.4 ± 7.8	–	–	–	0.793	1.786	A	10.9 ± 1.3
				0.027	4.39	20.4	*0.457 ± 0.055*			
HATLASJ090302.9−014127(SDP.17)	354.1 ± 7.2	338.8 ± 8.1	220.0 ± 8.6	0.988	0.83	21.7	0.9435	2.3049	A	>4.9
HATLASJ084933.4+021442(I13)	216.7 ± 7.5	248.5 ± 8.2	208.6 ± 8.6	0.777	1.65	20.4	–	2.410	D	
HATLASJ090740.0−004200(SDP.9)	477.6 ± 7.3	327.9 ± 8.2	170.6 ± 8.5	0.988	0.80	22.0	0.6129	1.577	A	8.8 ± 2.2
HATLASJ090311.6+003907(SDP.81)	133.2 ± 7.4	186.1 ± 8.2	165.2 ± 8.8	0.996	1.86	18.8	0.2999	3.042	A	16.0 ± 0.7
HATLASJ091840.8+023048(B13)	125.7 ± 7.2	150.7 ± 8.3	128.4 ± 8.7	–	–	–	–	2.581	C	
HATLASJ091304.9−005344(SDP.130)	118.2 ± 6.4	136.8 ± 7.4	104.3 ± 7.7	0.987	2.16	19.3	0.2201	2.6260	A	2.1 ± 0.3
GAMA-12$^{\rm h}$ field (53.6 deg^2)										
HATLASJ114637.9−001132(F12)	316.0 ± 6.6	357.9 ± 7.4	291.8 ± 7.7	0.990	0.42	21.7	1.2247	3.259	A	7.6 ± 1.5
				0.000	4.61	21.3	*0.470 ± 0.095*			
HATLASJ113526.2−014606(B13)	278.8 ± 7.4	282.9 ± 8.2	204.0 ± 8.6	–	–	–	–	3.1276	C	
HATLASJ121334.9−020323	211.0 ± 6.5	197.9 ± 7.5	129.9 ± 7.7	0.999	0.20	18.7	0.190[c]	*1.89 ± 0.35*	B	
HATLASJ121301.5−004922	136.6 ± 6.6	142.6 ± 7.4	110.9 ± 7.7	0.972	1.51	21.6	*0.191 ± 0.080*	*2.35 ± 0.40*	B	
HATLASJ120709.2−014702	143.2 ± 7.4	149.2 ± 8.1	110.3 ± 8.7	–	–	–	–	*2.26 ± 0.39*	C	
HATLASJ120319.1−011253	114.3 ± 7.4	142.8 ± 8.2	110.2 ± 8.6	–	–	–	–	*2.70 ± 0.44*	C	
HATLASJ115101.7−020024	183.5 ± 7.3	164.7 ± 8.0	108.7 ± 8.6	–	–	–	–	*1.81 ± 0.34*	C	
HATLASJ115112.2−012637	141.2 ± 7.4	137.7 ± 8.2	108.4 ± 8.8	0.996	0.45	20.2	0.426[c]	*2.22 ± 0.39*	B	
HATLASJ120127.6−014043	67.4 ± 6.5	112.1 ± 7.4	103.9 ± 7.7	–	–	–	–	*3.80 ± 0.58*	C	
HATLASJ120127.8−021648	207.9 ± 7.3	160.9 ± 8.2	103.6 ± 8.7	–	–	–	–	*1.50 ± 0.30*	C	
HATLASJ121542.7−005220	119.7 ± 7.4	135.5 ± 8.2	103.4 ± 8.6	–	–	–	–	*2.48 ± 0.42*	C	
HATLASJ115820.1−013752	119.8 ± 6.8	123.7 ± 7.7	101.5 ± 7.9	–	–	–	–	2.1911	C	
GAMA-15$^{\rm h}$ field (54.6 deg^2)										
HATLASJ142935.3−002836(M14)	801.8 ± 6.6	438.5 ± 7.5	199.8 ± 7.7	0.985	1.58	20.6	0.2184	1.027	A	10.8 ± 0.7
HATLASJ142413.9+022303(B12)	112.2 ± 7.3	182.2 ± 8.2	193.3 ± 8.5	0.986	0.74	22.1	0.595	4.243	A	4.6 ± 0.5
HATLASJ141351.9−000026(B13)	188.6 ± 7.4	217.0 ± 8.1	176.4 ± 8.7	0.980	1.12	22.2	0.5470	2.4782	A	>1.8
HATLASJ144608.6+021927	73.4 ± 7.1	111.7 ± 8.1	122.1 ± 8.7	–	–	–	–	*4.10 ± 0.61*	C	
HATLASJ144556.1−004853(B13)	126.7 ± 7.3	132.6 ± 8.4	111.8 ± 8.7	–	–	–	–	*2.51 ± 0.42*	C	
NGP field (170.1 deg^2)										
HATLASJ134429.4+303034(B13)	462.0 ± 7.4	465.7 ± 8.6	343.3 ± 8.7	0.987	0.43	21.9	0.6721	2.3010	A	11.7 ± 0.9
HATLASJ132630.1+334407(B13)	190.6 ± 7.3	281.4 ± 8.2	278.5 ± 9.0	0.922	2.16	21.3	0.7856	2.951	A	4.1 ± 0.3
HATLASJ125632.4+233627(B13)	209.3 ± 7.3	288.5 ± 8.2	264.0 ± 8.5	0.997	1.18	19.2	0.2551	3.565[a]	A	11.3 ± 1.7
HATLASJ132427.0+284449(B13,G13)	342.4 ± 7.3	371.0 ± 8.2	250.9 ± 8.5	–	–	–	0.997	1.676	A	>2.8
HATLASJ132859.2+292326(B13)	268.4 ± 6.5	296.3 ± 7.4	248.9 ± 7.7	–	–	–	–	2.778	C	
HATLASJ125135.3+261457(B13)	157.9 ± 7.5	202.3 ± 8.2	206.8 ± 8.5	–	–	–	–	3.675	A	11.0 ± 1.0
HATLASJ133008.5+245900(B13,C14)	271.2 ± 7.2	278.2 ± 8.1	203.5 ± 8.5	0.986	1.38	20.7	0.4276	3.1112[a]	A	13.0 ± 1.5
HATLASJ133649.9+291800(B13)	294.1 ± 6.7	286.0 ± 7.6	194.1 ± 8.2	–	–	–	–	2.2024	A	4.4 ± 0.8
HATLASJ132504.3+311534	240.7 ± 7.2	226.7 ± 8.2	164.9 ± 8.8	0.749	2.42	22.3	*0.58 ± 0.11*	*2.03 ± 0.36*	B	–
HATLASJ125759.5+224558	272.4 ± 7.3	215.0 ± 8.1	137.8 ± 8.7	0.985	1.14	21.0	*0.513 ± 0.021*	*1.53 ± 0.30*	B	–
HATLASJ133846.5+255054	159.0 ± 7.4	183.1 ± 8.2	137.6 ± 9.0	0.965	1.95	20.7	*0.42 ± 0.10*	*2.49 ± 0.42*	A	–
HATLASJ125652.4+275900	133.9 ± 7.5	164.1 ± 8.2	131.8 ± 8.9	0.925	1.20	21.6	–	*2.75 ± 0.45*	C	–
HATLASJ133413.8+260457	136.1 ± 7.2	161.1 ± 7.8	126.5 ± 8.4	–	–	–	–	*2.63 ± 0.44*	C	–
HATLASJ133542.9+300401	136.6 ± 7.2	145.7 ± 8.0	125.0 ± 8.5	0.477	3.13	21.5	0.980[d]	2.685[a]	A	–
HATLASJ133255.6+265528	192.5 ± 7.4	167.4 ± 8.1	116.6 ± 8.6	0.034	4.32	19.6	*0.070 ± 0.025*	*1.81 ± 0.34*	C	–
HATLASJ132419.0+320752	84.5 ± 6.8	116.0 ± 7.6	115.4 ± 8.0	–	–	–	–	*3.54 ± 0.54*	C	–
HATLASJ133255.7+342207	164.3 ± 7.5	186.8 ± 8.1	114.9 ± 8.7	–	–	–	–	*2.17 ± 0.38*	C	–
HATLASJ125125.8+254929	57.4 ± 7.4	96.8 ± 8.2	109.4 ± 8.8	0.970	1.62	21.2	*0.62 ± 0.10*	*4.47 ± 0.66*	B	–
HATLASJ134158.5+292833	174.4 ± 6.7	172.3 ± 7.7	109.2 ± 8.1	0.996	1.68	18.6	*0.217 ± 0.015*	*1.95 ± 0.35*	B	–
HATLASJ131540.6+262322	94.1 ± 7.4	116.1 ± 8.2	108.6 ± 8.7	–	–	–	–	*3.12 ± 0.49*	C	–
HATLASJ130333.1+244643	99.0 ± 7.2	111.5 ± 8.2	104.5 ± 8.7	–	–	–	–	*2.91 ± 0.47*	C	–
HATLASJ133038.2+255128	175.8 ± 7.4	160.3 ± 8.3	104.2 ± 8.8	0.983	0.792	21.6	*0.20 ± 0.15*	*1.82 ± 0.34*	B	–
HATLASJ130118.0+253708	60.2 ± 6.8	101.1 ± 7.7	101.5 ± 8.1	–	–	–	–	*4.08 ± 0.61*	C	–
HATLASJ134422.6+231951	109.6 ± 7.9	98.3 ± 9.1	101.4 ± 9.2	–	–	–	–	*2.58 ± 0.43*	C	–

Table 4 – *continued*

H-ATLAS IAU name	F_{250} (mJy)	F_{350} (mJy)	F_{500} (mJy)	reliab. SDSS-ID	sep(arcsec) SDSS-ID	r-mag SDSS-ID	z_{opt}	z_{sub-mm}	Lensing rank	μ_{sub-mm}
SGP field (269.5 deg^2)										
HATLASJ012407.3−281434	257.5 ± 6.0	271.1 ± 6.0	203.9 ± 6.8				–	*2.31 ± 0.40*	C	–
HATLASJ013840.4−281855	116.3 ± 5.7	177.0 ± 6.0	179.4 ± 7.1				–	*3.86 ± 0.58*	C	–
HATLASJ232531.3−302235	175.5 ± 4.3	227.0 ± 4.7	175.7 ± 5.7				–	*2.80 ± 0.46*	C	–
HATLASJ232419.8−323926	213.0 ± 4.4	244.2 ± 4.8	169.4 ± 5.8				–	*2.37 ± 0.40*	C	–
HATLASJ010250.8−311723	267.9 ± 5.2	253.1 ± 5.7	168.1 ± 7.1				–	*1.92 ± 0.35*	C	–
HATLASJ000912.7−300807	352.8 ± 5.4	272.6 ± 6.1	156.1 ± 6.8				–	*1.39 ± 0.29*	C	–
HATLASJ234418.1−303936	125.8 ± 5.1	185.5 ± 5.6	155.1 ± 7.0				–	*3.27 ± 0.51*	C	—
HATLASJ234357.7−351723	263.5 ± 5.3	223.0 ± 5.8	154.2 ± 7.0				–	*1.73 ± 0.33*	C	–
HATLASJ002624.8−341737	137.7 ± 5.2	185.9 ± 5.8	148.8 ± 6.8				–	*2.96 ± 0.48*	C	–
HATLASJ012046.4−282403	103.3 ± 5.7	149.8 ± 5.8	145.7 ± 7.4				–	*3.62 ± 0.55*	C	–
HATLASJ235827.6−323244	112.5 ± 4.6	148.0 ± 5.2	143.4 ± 6.1				–	*3.37 ± 0.52*	C	–
HATLASJ225844.7−295124	175.4 ± 5.2	187.0 ± 5.9	142.6 ± 7.5				–	*2.36 ± 0.40*	C	–
HATLASJ230815.5−343801	79.4 ± 5.4	135.4 ± 5.7	140.0 ± 7.0				–	*4.23 ± 0.63*	C	–
HATLASJ224805.3−335820	122.3 ± 5.7	135.5 ± 6.3	126.9 ± 7.2				–	*2.86 ± 0.46*	C	–
HATLASJ232623.0−342642	153.7 ± 4.4	178.3 ± 5.0	123.5 ± 6.2				–	*2.40 ± 0.41*	C	–
HATLASJ232900.6−321744	118.3 ± 4.7	141.2 ± 5.2	119.7 ± 6.4				–	*2.81 ± 0.46*	C	–
HATLASJ013239.9−330906	112.0 ± 5.5	148.8 ± 6.2	117.7 ± 7.0				–	*2.90 ± 0.47*	C	–
HATLASJ000007.4−334059	130.3 ± 5.4	160.1 ± 5.9	116.2 ± 6.5				–	*2.56 ± 0.43*	C	–
HATLASJ005132.8−301848	164.6 ± 5.4	160.2 ± 5.8	113.0 ± 7.2				–	*2.05 ± 0.37*	C	–
HATLASJ225250.7−313657	127.4 ± 4.2	138.7 ± 4.9	111.4 ± 5.9				–	*2.49 ± 0.42*	C	–
HATLASJ230546.2−331038	76.8 ± 5.6	110.9 ± 5.9	110.4 ± 7.0				–	*3.67 ± 0.56*	C	–
HATLASJ000722.1−352014	237.3 ± 5.2	192.8 ± 5.6	107.5 ± 6.6				–	*1.46 ± 0.30*	C	–
HATLASJ013951.9−321446	109.0 ± 4.9	116.5 ± 5.3	107.1 ± 6.2				–	*2.73 ± 0.45*	C	–
HATLASJ003207.7−303724	80.3 ± 5.0	106.2 ± 5.2	105.8 ± 6.3				–	*3.45 ± 0.53*	C	–
HATLASJ004853.2−303109	118.1 ± 4.5	147.3 ± 5.0	105.4 ± 6.0				–	*2.59 ± 0.43*	C	–
HATLASJ005132.0−302011	119.3 ± 5.0	121.0 ± 5.8	102.0 ± 6.6				–	*2.42 ± 0.41*	C	–
HATLASJ224207.2−324159	73.0 ± 5.5	88.1 ± 6.2	100.8 ± 7.7				–	*3.60 ± 0.55*	C	–
HATLASJ013004.0−305513	164.4 ± 4.3	147.5 ± 5.1	100.6 ± 5.9				–	*1.84 ± 0.34*	C	–
HATLASJ223753.8−305828	139.1 ± 4.9	144.9 ± 5.1	100.6 ± 6.2				–	*2.17 ± 0.38*	C	–
HATLASJ012415.9−310500	140.4 ± 5.4	154.5 ± 5.7	100.3 ± 7.0				–	*2.20 ± 0.38*	C	–

Notes. B13 = Bussmann et al. (2013); I13 = Ivison et al. (2013); F12 = Fu et al. (2012); M14 = Messias et al. (2014); B12 = Bussmann et al. (2012); G13 = George et al. (2013); C14 = Calanog et al. (2014).
[a]From CARMA (Riechers et al., in preparation).
[b]from PdBI (Yang et al. 2016).
[c]from NTT (Amber 2015).
[d]Stanford et al. (2014).

Magnification factors, μ, have been derived from the lens modelling of the high-resolution imaging data shown in Fig. 3. Those obtained at sub-mm wavelengths from SMA (and ALMA for HATLAS090311.6+003907 and HATLASJ142935.3-002836) data are reported in Table 4. For three objects, the magnification factor derived by Bussmann et al. (2013) has been replaced by a lower limit: it is the case of the two cluster-scale lenses, i.e. HATLASJ141351.9−000026 and HATLASJ132427.0+284449, which were modelled by Bussmann et al. as if they were galaxy-scale lenses, and SDP.17, for which SMA did not resolve the multiple images. The measured values[4] of μ are in the range $\mu \sim 5$–15, consistent with expectations (Negrello et al. 2007). As we will discuss in Section 4, the statistics of lensed galaxies (i.e. the sub-mm bright number counts) can also provide information on the typical magnification experienced by the background source population to be compared with the measured values of μ.

Only one object in our sample of candidate lensed galaxies, HATLASJ084933.4+021442, has been so far confirmed to not be a strongly lensed galaxy. It is indeed a binary system of Hyper Luminous Infrared Galaxies[5] (HyLIRGs) at $z = 2.410$ reported by Ivison et al. (2013), which is believed to represent the early stage in the formation of the core of a massive galaxy cluster.

3.3 Colours and redshifts

A colour–colour plot based on the *Herschel*/SPIRE photometry is shown in Fig. 4 for candidate lensed galaxies (dots), local galaxies (squares) and blazars (triangles) with $F_{500} \geq 100$ mJy. In the same figure, we have delimited the regions occupied by objects with SED peaking at ∼350 μm (i.e. with $F_{250}/F_{350} < 1$ and $F_{350}/F_{500} > 1$; '350 μm peakers') and by objects with SED rising from 250 to 500 μm (i.e. with $F_{250} \leq F_{350} \leq F_{500}$; '500 μm risers'). There is clearly a bimodal distribution in the F_{250}/F_{350} values, with candidate lensed galaxies having significantly 'redder' colours (i.e. higher emission at 350 μm than at 250 μm) compared to local

[4] The magnification factors are derived by assuming either an analytic Sérsic profile for the light profile of the background galaxy (Bussmann et al. 2013) or a pixelized surface brightness distribution (e.g. Dye et al. 2014).

[5] One of the two HyLIRGs is claimed to be weakly lensed (i.e. $\mu \sim 1.5$) by a foreground lenticular galaxy.

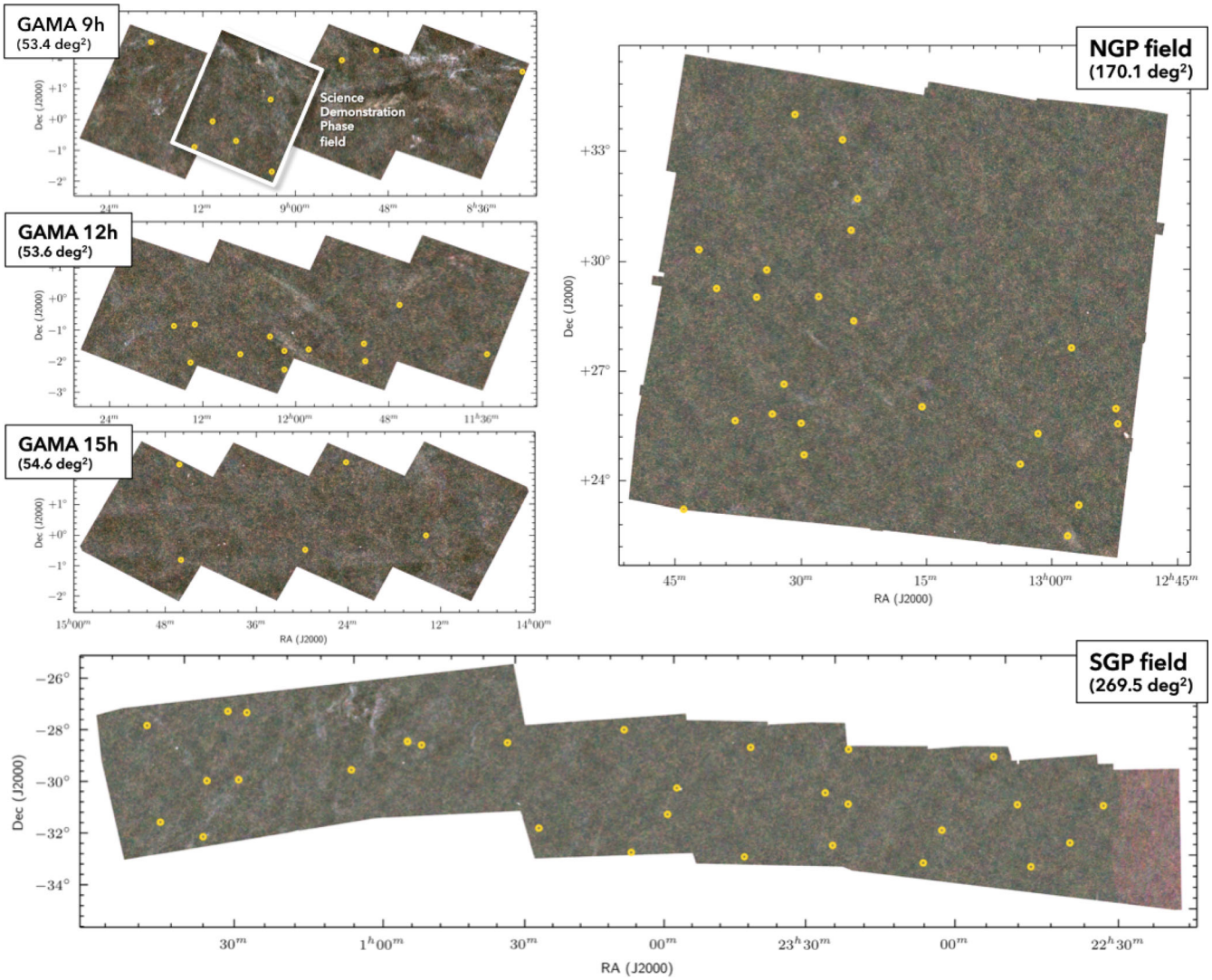

Figure 2. *Herschel*/SPIRE colour maps of the *H*-ATLAS fields. The yellow circles mark the position of the 80 candidate lensed galaxies with $F_{500} \geq 100$ mJy.

galaxies. This is consistent with the former lying at much higher redshift (i.e. $z \gtrsim 1$). In fact, the majority of the candidate lensed galaxies are classified as 350 μm peakers. The candidate lensed galaxy with the 'bluest' colours, i.e. with $F_{250}/F_{350} > 1.7$, is HATLASJ142935.3−002836, our lowest redshift ($z = 1.027$) confirmed lensed source (Messias et al. 2014, see Fig. 3).

Pearson et al. (2013) have used a sub-set of 40 *H*-ATLAS sources with spectroscopic redshifts in the range $0.5 < z < 4.2$ to construct an empirical SED for high-redshift *Herschel*-selected sources to be used to estimate photometric redshifts from *Herschel*/SPIRE data. The template is the sum of two modified blackbody spectra with temperatures $T_{\rm cold} = 23.9$ K and $T_{\rm hot} = 46.9$ K, and dust emissivity index fixed to $\beta = 2$. The ratio between the normalization of the two components is 30.1. In Fig. 4, we show the track of the empirical SED for redshifts from 0.5 to 4.5 in steps of 0.5. The colours of the candidate lensed galaxies are consistent with them being in the redshift range 1.5–4.5. Their photometric redshifts, derived by fitting the *Herschel*/SPIRE photometry with the Pearson et al. (2013) template, are listed in Table 4, in italic style. The errors are calculated as $0.12 \times (1 + z_{\rm phot})$, 0.12 being the rms scatter in the $(z_{\rm phot} - z_{\rm spec})/(1 + z_{\rm spec})$ values as measured by Pearson et al. for sources with $z_{\rm spec} > 1$.

In the lower panel of Fig. 5, we show the redshift distribution of the candidate lensed galaxies with $F_{500} \geq 100$ mJy, with photometric redshifts replaced by spectroscopic ones where available. The Ivison et al. (2013) source is not included in the plot, as it is known to not be strongly lensed. The distribution is derived by performing 10 000 simulations. Each time, the redshift of the sources is resampled at random, from a Gaussian probability distribution with a mean equal to the measured photometric/spectroscopic redshift and dispersion equal to the associated error. The simulated redshifts are then binned into a histogram and the mean value in each bin is taken as the estimate of the number of objects in that bin. Error bars, corresponding to the 68 per cent confidence interval, are derived following the prescriptions of Gehrels et al. (1986) for Poisson statistics. The median redshift is $z_{\rm median} = 2.53$. Similar median redshifts are obtained for the spectroscopic redshift sample and the photometric redshift sample alone, i.e. $z_{\rm median} = 2.49$ and 2.54, respectively (the two distributions are shown in the upper panel of Fig. 5). The measured redshift distribution is consistent with predictions based on the physical model of Cai et al. (2013) once combined with the lensing formalism of Lapi et al. (2012) for maximum magnifications in the range 10–15 (see Section 4.2 for details on the modelling).

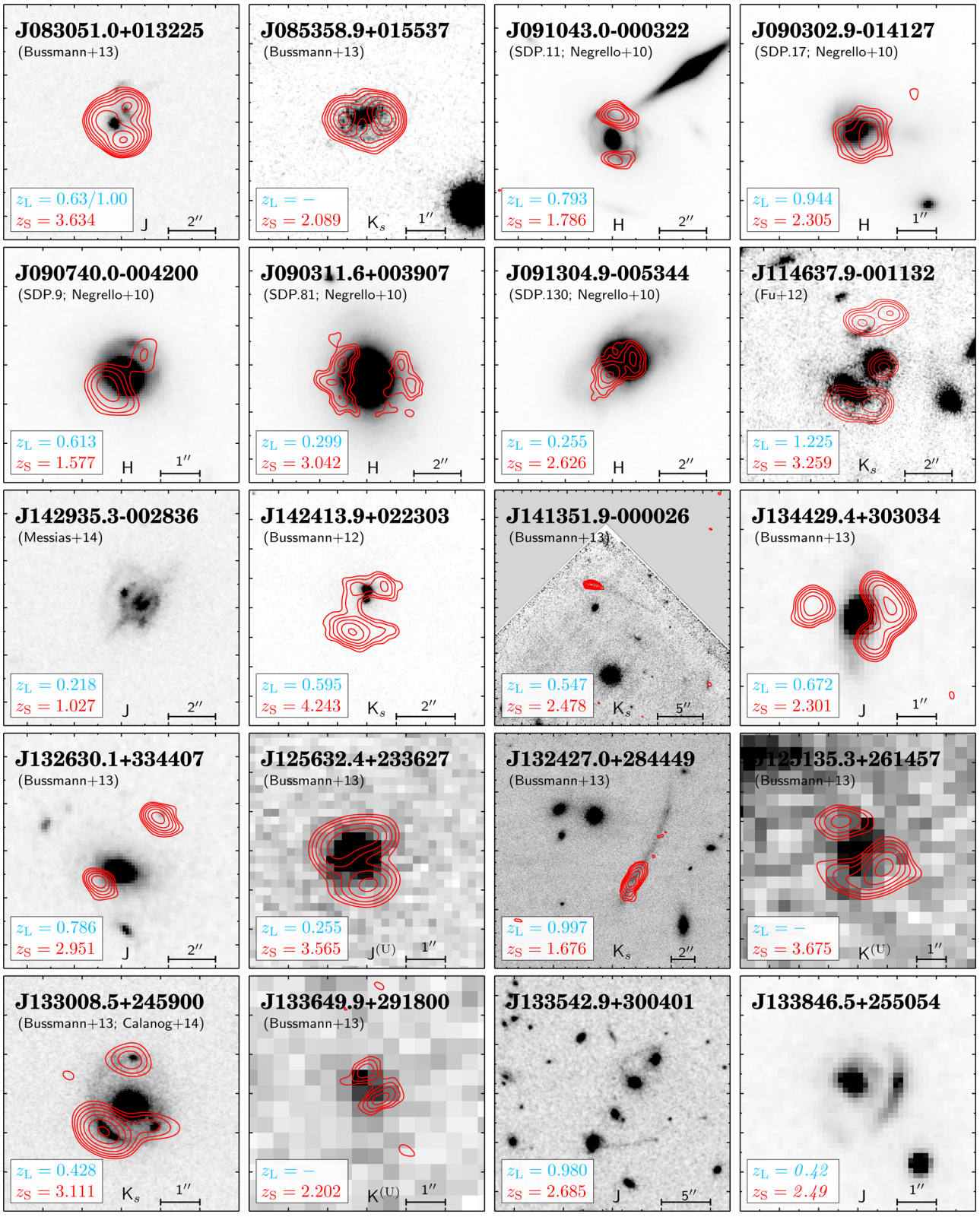

Figure 3. Postage stamps of the 20 confirmed lensed galaxies in the *H*-ATLAS fields. SMA 880 μm signal-to-noise ratio contours are superimposed to either the *HST*/WFC3/*F*110*W* (*J*-band), or *HST*/WFC3/*F*160*W* (*H*-band), or *Keck* K_s-band or UKIDSS *J*/*K*-band image (the latter is denoted by the apex $^{(U)}$). The redshifts of the lens, z_L, and the redshift of the background galaxy, z_S, are shown at the bottom of each stamp (in italic style when photometrically determined).

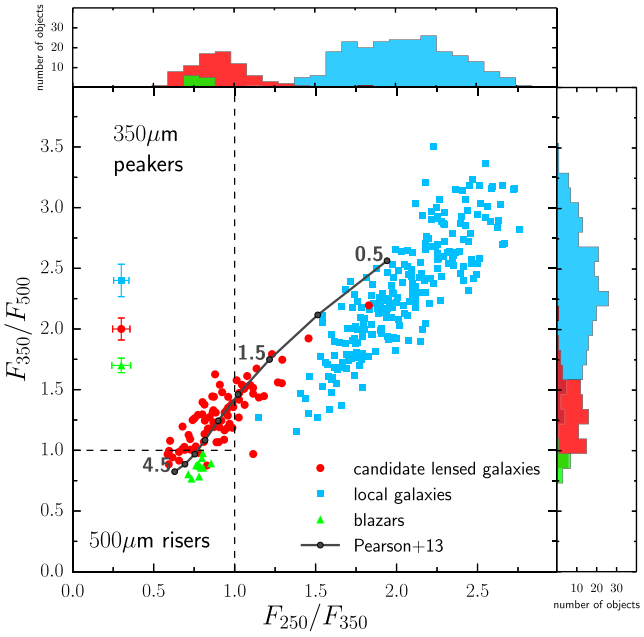

Figure 4. *Herschel*/SPIRE colour–colour diagram of candidate lensed galaxies (red dots), local galaxies (blue squares) and blazars (green triangles) with $F_{500} \geq 100$ mJy identified in the *H*-ATLAS fields. The histograms show the number of the source as a function of flux-density ratio. Typical error bars for the different source populations are shown on the left. The black line is the track of the Pearson et al. (2013) empirical template for redshifts in the range [0.5,4.5] in steps of 0.5 (in increasing order from the top-right to the bottom-left corner), as marked by the black dots.

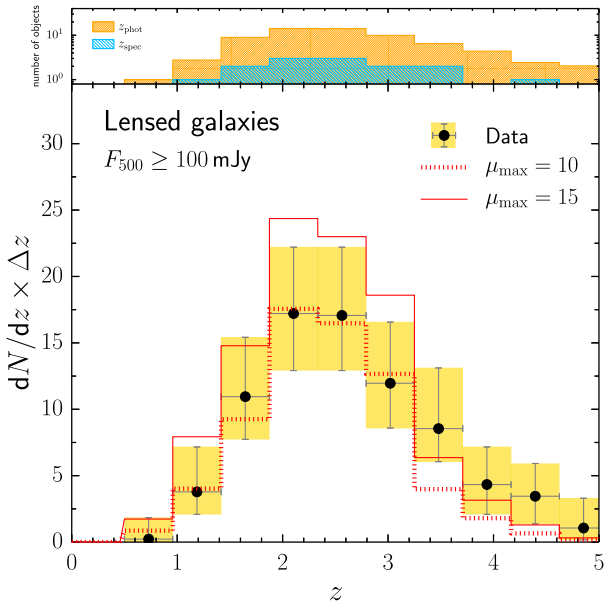

Figure 5. Redshift distribution of the candidate lensed galaxies with $F_{500} \geq 100$ mJy identified in the *H*-ATLAS. Upper panel: distribution of the photometric redshift sample (orange) and of the spectroscopic redshift sample (blue). Lower panel: distribution of the photometric+spectroscopic redshift sample (dots with error bars). The shaded region represents the 68 per cent confidence interval assuming Poisson statistics (Gehrels 1986). The curves are predictions based on the galaxy formation and evolution model of Cai et al. (2013) coupled with the lensing formalism of Lapi et al. (2012), assuming different maximum magnifications: $\mu_{max} = 10, 15$.

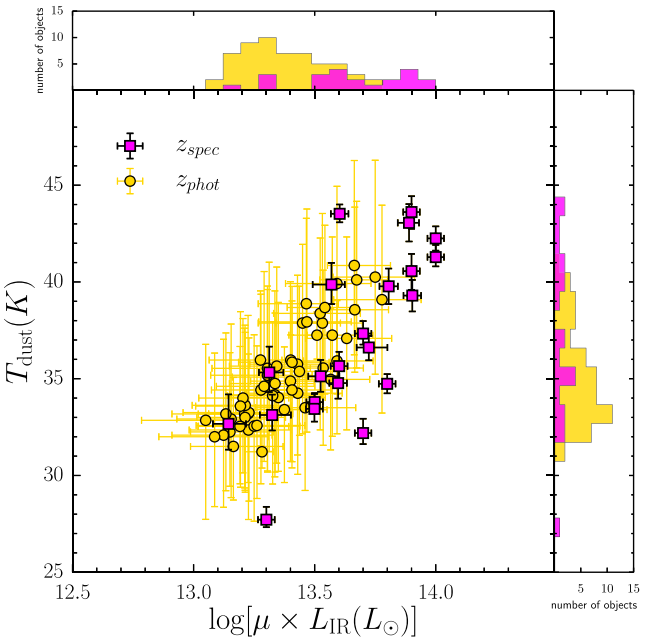

Figure 6. Dust temperature versus IR luminosity (8−−1000 μm, not corrected for lensing) of the candidate lensed galaxies extracted from the *H*-ATLAS fields, excluding the Ivison et al. (2013) source. Squares correspond to objects with spectroscopic redshift while the dots indicate objects with photometric redshift. Error bars correspond to the 68 per cent confidence interval and take into account uncertainties on both the redshifts and the *Herschel* photometry. The IR luminosity and the dust temperature are derived assuming an optically thin greybody model with dust emissivity index fixed to $\beta = 1.5$.

We use the redshift information to derive the IR luminosity, L_{IR} (integrated over the rest-frame wavelength range 8−−1000 μm), of our candidate lensed galaxies. We assume a single temperature, optically thin, modified blackbody spectrum with dust emissivity index $\beta = 1.5$ (Bussmann et al. 2013; Nayyeri et al. 2016) and we fit it to the *Herschel* photometry of each source. The IR luminosity and dust temperature, T_{dust}, are kept as free parameters. In order to account for the uncertainty on the photometric/spectroscopic redshift, as well as that on the photometry, we perform for each source 1000 simulations by resampling at random the distributions of redshift values and measured flux densities, both assumed to be Gaussian. The final values of L_{IR} and T_{dust}, shown in Fig. 6, are obtained as the median of the derived distributions of 1000 best-fitting values. All the galaxies in the sample appear to be HyLIRGs (i.e. $L_{IR} \geq 10^{13}$ L$_\odot$). However, with an expected typical magnification of ∼5–15 (Lapi et al. 2012; Bussmann et al. 2013; Dye et al. 2014, see also Fig. 9), most of them are likely to be *intrinsically* ultraluminous infrared galaxies ($10^{12} \leq L_{IR}/L_\odot \leq 10^{13}$). The median value of the dust temperature is $T_{dust} = 34.6$, consistent with what was found for other sub-mm/mm-selected unlensed (Magnelli et al. 2012) and lensed (Weiß et al. 2013; Cañameras et al. 2015; Nayyeri et al. 2016) galaxies.

3.4 Optical and near-IR counterparts

Bourne et al. (2016) and Furlanetto et al. (2016) used a likelihood-ratio (LR) technique (Richter et al. 1975; Sutherland & Saunders 1992; Ciliegi et al. 2003) to identify SDSS counterparts with $r < 22.4$ to the *H*-ATLAS sources in the GAMA fields and in the

NGP field, respectively. This technique exploits the knowledge of the intrinsic positional uncertainty of the sources, as well as the magnitude distributions of true counterparts and background sources to assign a probability ('reliability', R) to each potential match, thus allowing us to distinguish robust counterparts from chance alignments with background sources. We consider an optical source to be reliable counterpart to the *Herschel*/SPIRE detection if $R > 0.8$. We do not expect lensed DSFGs to be visible in the optical above the adopted r-band limit, because of the combined effect of high redshift and dust obscuration. However, in gravitational lensing systems, the foreground object acting as the lens, usually an elliptical galaxy at redshifts $z \sim 0.3$–0.8 (see Table 4), is likely to be detected at optical and/or near-IR wavelengths. We find that nine of the yet to be confirmed lensed galaxies have a reliable optical counterpart in SDSS, but the photometric redshift of the SDSS source (where available) is much lower than the one derived from the *Herschel*/SPIRE photometry, as reported in Table 4. This is consistent with the lensing scenario where the lens is detected in the optical while the background galaxy entirely contributes to the far-IR/sub-mm emission. The estimated high reliability of the association between two distinct objects is actually determined by gravitational lensing, which physically relates them. This effect was already observed in the first sample of five lensed galaxies discovered by Negrello et al. (2010).

In Appendix A, we show optical (SDSS or KiDS) to near-IR (UKIDSS-LAS or VIKING or *HST*/*F*110*W* where available) postage stamps images of the yet to be confirmed lensed galaxies. The spatial resolution ranges from 0.14 arcsec for *HST*/*F*110*W*, to $\lesssim$0.7 arcsec for KiDS r-band, 1.4 arcsec for SDSS r-band, and $\lesssim$1 arcsec for VIKING and UKIDSS-LAS. The reliable optical counterparts are marked in the optical r-band images. No LR analysis has been performed on near-IR catalogues yet; however, we note that most of our candidate lensed galaxies have a near-IR source (or even more than one in some cases) within a 5 arcsec distance, likely to be the lens, with eventually some contribution from the background galaxy (see e.g. Negrello et al. 2014). There is an ongoing effort to measure the redshift of these near-IR counterparts to confirm that they lie at $z \lesssim 1$.

Based on available imaging and spectroscopic information, we provide in Table 4 a *lensing rank* for each object as follows.

A = *The Herschel*/SPIRE *source is confirmed to be strongly lensed* according to the detection of multiple images or arcs with *HST*/*Keck*/SMA and/or the availability of spectroscopic redshifts for both the lens and the background galaxy, indicating the presence of two distinct objects along the line of sight.

B = *The Herschel/* SPIRE *source is likely to be lensed* based on the difference in redshift between the optical/near-IR ID and the sub-mm detection, although at least one of the two redshifts is photometric.

C = *The nature of the Herschel*/SPIRE *source is unclear* because of the lack of a reliable optical/near-IR counterpart, which may indicate that the lens is particularly faint and/or lying at $z > 1$, or that the sub-mm source is an unlensed HyLIRG or a cluster of HyLIRGs.

D = *The Herschel/SPIRE source is not strongly lensed*.

To summarize, in our sample there are 20 confirmed lensed galaxies (i.e. rank A), eight sources have been assigned rank B, while 51 have rank C. Only one object has been proven, so far, to not be strongly lensed (i.e. rank D).

4 NUMBER COUNTS

In this section, we derive the number counts of the candidate lensed galaxies and compare them with model predictions.

4.1 Measurements

The integral number counts of the candidate lensed galaxies are shown in Fig. 7 for each of the *H*-ATLAS fields: top panels for the three equatorial GAMA fields; bottom-left and bottom-middle panels for the NGP and SGP fields, respectively. Error bars and upper limits correspond to the 68 per cent confidence interval, assuming Poisson statistics. The GAMA 9$^{\rm h}$ field and the NGP field appear to be particularly rich in lensed galaxies with $F_{500} \gtrsim 200$ mJy. On the contrary, the SGP field is short of such bright sources. In fact, only one candidate lensed galaxy with $F_{500} \geq 200$ mJy is found in the SGP field, while 13 have been identified in the other fields (most of which are already confirmed lensed galaxies). In the bottom-right panel of the same figure, we show the comparison between the number counts extracted from the SGP field and those derived by combining the three equatorial fields with the NGP field. In this case, the error bars and the upper limits have been drawn to represent the 95 per cent confidence interval. It is clear that, despite the large difference in number density for $F_{500} \gtrsim 150$ mJy, the two samples are still consistent with each other at the $\sim 2\sigma$ level. The observed fluctuations are also consistent with the results of simulations based on the modelled lensed number counts, as discussed in the Section 4.2.

Once we combine the samples from all the five *H*-ATLAS different fields, the measured number counts, shown in Fig. 8 and reported in Table 5, are in very good agreement with those derived from HeLMS+HerS (Nayyeri et al. 2016) for $F_{500} \gtrsim 125$ mJy. At fainter flux densities, Nayyeri et al. report 77 candidate lensed galaxies with $F_{500} \geq 100$ mJy over an area of 370 deg^2, to be compared with the 79 we find over the 600 deg^2 of the full *H*-ATLAS. This difference in number density, i.e. 0.21 deg^{-2} versus 0.13 deg^{-2}, is still consistent with Poisson fluctuations at the $\sim 2\sigma$ level.

4.2 Modelling

Given the *true* number density of unlensed DSFGs per unit logarithmic interval in flux density, $({\rm d}N/{\rm dlog}F)_{\rm T}$, the corresponding number density of lensed DSFGs is computed as (e.g. Lima, Jain & Devlin 2010; Lapi et al. 2012)

$$\left(\frac{{\rm d}N}{{\rm dlog}F}\right)_{\rm L}(F) = \int_{\mu_{\rm min}}^{\mu_{\rm max}} \left(\frac{{\rm d}N}{{\rm dlog}F}\right)_{\rm T}(F/\mu)p(\mu){\rm d}\mu, \quad (1)$$

where F is the *measured* flux density of the sources, and $p(\mu)$ is the probability that a source has its flux boosted by a factor μ as an effect of lensing.

In general, the probability distribution of the magnifications depends on the redshift of the source, $z_{\rm S}$, with higher redshift objects being more likely lensed than lower redshift ones (as a consequence of the higher optical depth for lensing). Therefore, a more accurate version of equation (1) is

$$\left(\frac{{\rm d}N}{{\rm dlog}F{\rm d}z_{\rm S}}\right)_{\rm L}(F, z_{\rm S}) = \int_{\mu_{\rm min}}^{\mu_{\rm max}} \left(\frac{{\rm d}N}{{\rm dlog}F{\rm d}z_{\rm S}}\right)_{\rm T}(F/\mu)p(\mu, z_{\rm S}){\rm d}\mu, \quad (2)$$

with the number densities now given per unit interval in redshift (of the source) as well as per unit logarithmic interval in flux

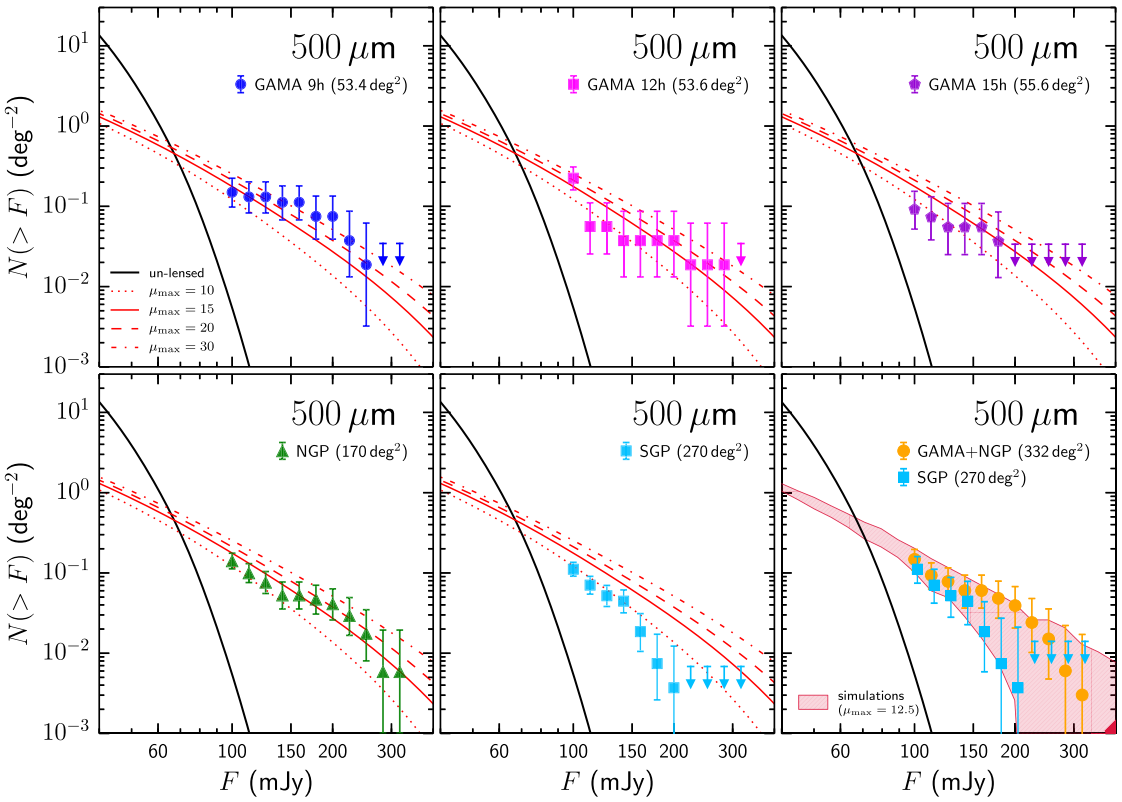

Figure 7. Integral number counts of the candidate lensed galaxies with $F_{500} \geq 100$ mJy identified in the five *H*-ATLAS fields: GAMA 9$^{\rm h}$ (top-left), GAMA 12$^{\rm h}$ (top-middle), GAMA 15$^{\rm h}$ (top-right), NGP (bottom-left) and SGP (bottom-middle). The bottom-right panel shows the comparison between the number counts measured in the SGP field and those derived by combining the three GAMA fields with the NGP fields. Error bars and upper limits correspond to the 68 per cent confidence interval assuming Poisson statistic (Gehrels 1986), with the exception of the bottom-right panel where they are shown at the 95 per cent confidence level. In all panels, the solid black curve is the prediction for the abundance of unlensed DSFGs at $z \gtrsim 1.5$, based on the model of Cai et al. (2013). The red curves show the predicted number counts of lensed galaxies for different values of the maximum magnification, $\mu_{\rm max}$, experienced by the background sources, from 10 to 30. The mass profile of the lenses is assumed to be the superposition of an NFW profile (for the dark-matter component) and a de Vaucouleurs profile (accounting for baryons), as described in Lapi et al. (2012). More details are given in Section 4.2. The shaded region in the bottom-right panel illustrates the variation in the number density of lensed galaxies based on a set of 100 simulations performed over an area of 300 deg^2 and assuming $\mu_{\rm max} = 12.5$.

density. Here, we focus on the *strong* lensing regime, which occurs when multiple images of the background source are formed. The typical separation between multiple images is of the order of one to a few arcseconds. Such angular scales are below the resolution capabilities of *Herschel* which, in the case of a lensing event, can only measure the summed flux of the multiple images. For this reason, we will only consider the *total* magnification, $\mu_{\rm tot}$, experienced by a source, i.e. the sum of the modulus of the magnifications of the individual images. In equation (2), the minimum value of μ in the integration is fixed to the lowest value of $\mu_{\rm tot}$, which corresponds to the formation of multiple images. For lenses with a mass profile described by a Singular Isothermal Sphere model – as supported by the modelling of individual lensing systems (e.g. Dye et al. 2014) – the strong lensing regime is achieved when $\mu_{\rm tot} \geq 2$. Therefore, we set $\mu_{\rm min} = 2$. On the other hand, the value of $\mu_{\rm max}$ mainly depends on the intrinsic angular size of the background source: in general, the more compact the source, the higher the maximum magnification that can be achieved (see e.g. fig. 8 of Lapi et al. 2012). Perrotta et al. (2002) showed that for a source in the redshift range $z = 1$–4, with typical size $\simeq$1–10 kpc, consistent with observations of the dust-emitting region in DSFGs (e.g. Riechers et al. 2013, 2014; De Breuck et al. 2014; Simpson et al. 2014, 2015; Hodge et al. 2015, 2016; Ikarashi et al. 2015; Lindroos et al. 2016), the value of $\mu_{\rm tot}$ lies in the range 10–30 (see also Lapi et al. 2012). In the following, we work out predictions for different values for $\mu_{\rm max}$ in the range 10–30.

The function $p(\mu, z_{\rm S})$ depends on several factors: the distribution in mass and in redshift of the lenses and their mass profile. For a given lens of mass $M_{\rm L}$ and redshift $z_{\rm L}$, and a given redshift of source $z_{\rm S}$, one can define, in the source plane, the cross-section, $\Sigma(>\mu|M_{\rm L}, z_{\rm L}, z_{\rm S})$, for lensing events with total magnification $>\mu$, i.e. the area containing all the source positions for which $\mu_{\rm tot} > \mu$. In the strong lensing regime, the probability $P(>\mu|z_{\rm S})$ that a source is magnified by a value higher than μ is significantly lower than unity (as multiple images are only formed when the source and the lens are sufficiently well aligned), and it is very unlikely that the source is lensed by more than one foreground mass (i.e. 'non-overlapping' cross-sections approximation). In this regime, the probability $P(>\mu|z_{\rm S})$ is just (e.g. Peacock 1982)

$$P(>\mu|z_{\rm S}) = \int_{z_{\rm L}^{\rm min}}^{z_{\rm L}^{\rm max}} \int_{M_{\rm L}^{\rm min}}^{M_{\rm L}^{\rm max}} \Sigma(>\mu|M_{\rm L}, z_{\rm L}, z_{\rm S}) \frac{{\rm d}N_{\rm L}}{{\rm d}M_{\rm L}{\rm d}z_{\rm L}} {\rm d}M_{\rm L}{\rm d}z_{\rm L}, \quad (3)$$

where ${\rm d}N_{\rm L}/{\rm d}M_{\rm L}{\rm d}z_{\rm L}$ is the number density of the lenses per unit interval in mass and in redshift. The (differential) probability distribution of the magnifications can then be obtained by differentiating, i.e. $p(\mu|z_{\rm S}) = -{\rm d}P(>\mu|z_{\rm S})/{\rm d}\mu$. The total mass distribution

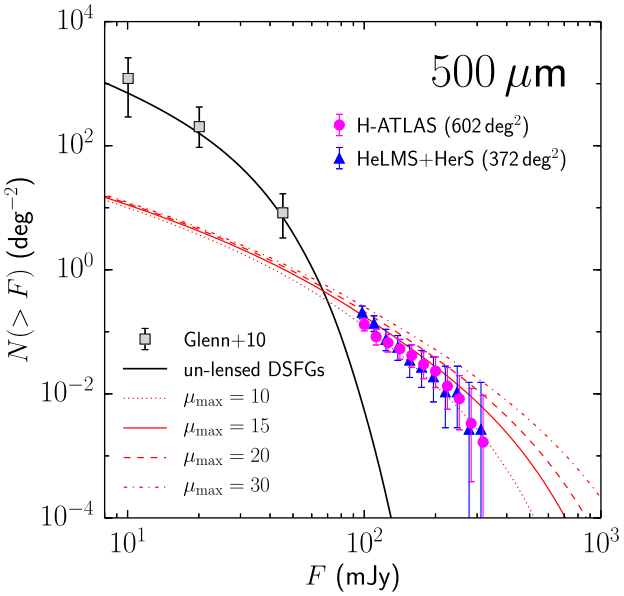

Figure 8. Integral number counts of the candidate lensed galaxies with $F_{500} \geq 100$ mJy identified in all the *H*-ATLAS fields (purple dots) compared with the number counts of candidate lensed galaxies derived by Nayyeri et al. (2016) from HeLMS+HerS (blue triangles). Error bars correspond to the 95 per cent confidence interval. For clarity, a small offset in flux density have been applied to the *H*-ATLAS data. The meaning of the curves is the same as in Fig. 7. The squares represent measurements of the number density of unlensed DSFGs derived from P(D) analysis (Glenn et al. 2010).

Table 5. Integral number counts of candidate lensed galaxies with $F_{500} \geq 100$ mJy in the *H*-ATLAS fields. The quoted errors on the number counts correspond to the 68 per cent confidence interval.

$\log[F_{500}/\mathrm{mJy}]$	$N(>F_{500}) \times 10^{-3}$ (deg^{-2})
2.000	131^{+17}_{-15}
2.038	96^{+14}_{-13}
2.075	73^{+13}_{-11}
2.113	62^{+12}_{-10}
2.150	53^{+11}_{-9}
2.188	47^{+11}_{-9}
2.225	$38.3^{+9.8}_{-7.9}$
2.263	$28.3^{+8.7}_{-6.8}$
2.300	$25.0^{+8.3}_{-6.4}$
2.338	$16.6^{+7.1}_{-5.2}$
2.375	$11.6^{+6.3}_{-4.3}$
2.413	$8.3^{+5.6}_{-3.6}$
2.450	$3.3^{+4.4}_{-2.1}$
2.488	$1.7^{+3.8}_{-1.4}$
2.525	$1.7^{+3.8}_{-1.4}$

of the lenses is described by the mass function of the dark-matter haloes derived from *N*-body simulation (e.g. Sheth & Tormen 1999). Therefore, the main uncertainty in the modelling of p is related to the choice of the cross-section $\Sigma(>\mu|M_{\rm L}, z_{\rm L}, z_{\rm S})$), which strictly depends on the mass profile of the lenses. A Singular Isothermal Ellipsoid (SIE; Kormann, Schneider & Bartelmann 1994) model pro-

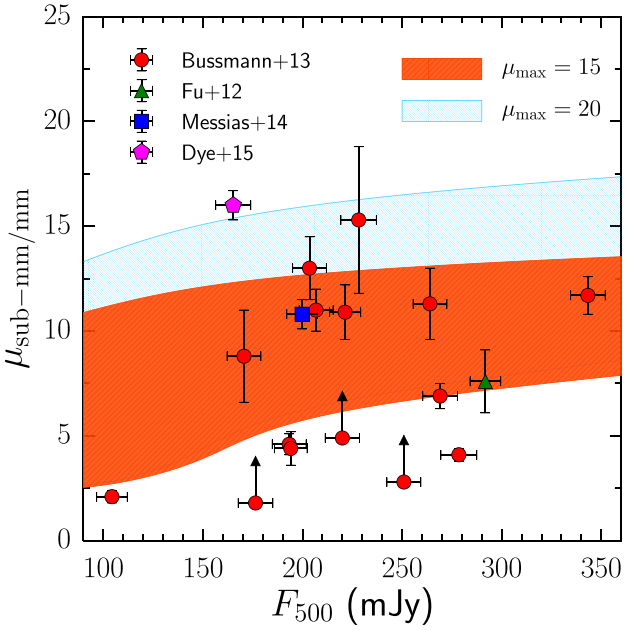

Figure 9. Magnification factors derived from high-resolution sub-mm/mm imaging of the confirmed lensed galaxies in the GAMA and NGP fields, compared with model predictions (Lapi et al. 2012 and Cai et al. 2013) for $\mu_{\rm max} = 15$ and 20. The shaded region shows the 68 per cent confidence interval around the median value of the probability distribution of the magnifications. The range of maximum magnifications suggested by the data is consistent with that inferred from the number counts of candidate lensed galaxies with $F_{500} \gtrsim 150$ mJy in the GAMA and NGP fields (see Fig. 7).

vides a good description of galaxy-scale lensing events, i.e. events where the lensing mass is associated with one single galaxy, typically an elliptical (Barnabè et al. 2011, and references therein), and of the corresponding image separation distribution (see e.g. fig. 10 of More et al. 2012). As shown by, e.g. Lapi et al. (2012), the SIE profile results from the combination of a Navarro–Frank–White (NFW) profile for the dark-matter distribution and a de Vaucouleurs profile for the distribution of baryons in elliptical galaxies. Here, we adopt the NFW plus de Vaucouleurs model by Lapi et al. to work out the probability distribution of the magnifications. For the dark-matter component, we adopt the concentration parameter derived by Prada et al. (2012) from numerical simulation, as a function of the dark-matter halo mass and redshift. We assume a dark-matter-to-baryon mass ratio $M_{\rm DM}/M_{\rm baryons} = 30$ and a virialization redshift $z_{\rm vir} = 3$ for the lens. These choices are consistent with observations of early-type galaxies (see Lapi et al. 2012, and references therein). We refer the reader to the Lapi et al. paper for a discussion of how the probability distribution of magnifications and the lensed number counts are affected by different choices of these parameters. For the number counts of unlensed DSFGs, we assume the model of Cai et al. (2013) which accurately fits a broad variety of data: multifrequency and multi-epoch luminosity functions of galaxies and AGN, redshift distributions, number counts (total and per redshift bins). The derived model predictions for different values of the maximum magnification, in the range 10–30, are shown in Figs 7 and 8. The number counts of the whole sample of candidate lensed galaxies (Fig. 8), as well as the redshift distribution (Fig. 5), suggest $\mu_{\rm max} \sim$ 10–15, although in the GAMA 9$^{\rm h}$ and NGP fields higher values of the maximum magnification, i.e. $\mu_{\rm max} \gtrsim$ 15–20, are in better agreement with the observations for $F_{500} \gtrsim 150$ mJy. As shown in Fig. 9, these values of $\mu_{\rm max}$ are consistent with the magnification

factors derived from the modelling of high-resolution sub-mm/mm imaging data of sub-mm-selected lensed galaxies (e.g. Swinbank et al. 2010; Bussmann et al. 2013, 2015; Dye et al. 2015; Spilker et al. 2016).

Using our theoretical models, we have investigated the level of fluctuations observed in the number density of candidate lensed galaxies between the GAMA+NGP and SGP fields. To do so, we have run a set of 100 simulations, over an area of 300 deg^2, by resampling at random the model luminosity function of DSFGs and by assigning to each simulated object a probability of being strongly lensed, and its corresponding magnification factor, according to the theoretical probability distribution of magnifications. We have assumed $\mu_{\rm max} = 12.5$, the mean value of the maximum magnifications suggested by the data, i.e. 10–15 (see Fig. 8). The range of integral number densities of lensed galaxies produced by the simulations is shown by the red shaded region in the bottom-right panel of Fig. 7. Large fluctuations in the number of the brightest lensed galaxies, as those observed in the GAMA+NGP versus SGP field, are quite rare, but not unlikely to occur. In fact, in two simulated catalogues (i.e. 2 per cent of the total), only one lensed source is detected above 200 mJy, while three simulated samples (i.e. 3 per cent of the simulations) contain at least 12 sources[6] with $F_{500} \geq 200$ mJy. Overall, we find a good agreement between the results of the simulations and the observations.

5 CONCLUSIONS

We have presented a catalogue of 80 candidate lensed galaxies with $F_{500} \geq 100$ mJy selected from the ∼600 deg^2 of the full *H*-ATLAS. 20 of them are confirmed to be lensed systems based on available optical to sub-mm/mm spectroscopic and high-resolution imaging data. One source was found to be a binary system of HyLIRGs. Other eight sources are very likely to be lensed based on the presence of two distinct objects along the same line of sight as suggested by the estimated photometric redshifts. The remaining candidate lensed galaxies still await follow-up observations to confirm their nature.

The number density of our candidate lensed galaxies is in agreement with expectations based on a physical model for the unlensed DSFG population coupled with a NFW plus de Vaucouleurs model for the mass profile of the lenses, assuming a maximum magnification in the range 10–20. These values of $\mu_{\rm max}$ are in agreement with the magnification factors estimated from the lens modelling and source reconstruction of individual lensed DSFGs. We observe quite a large fluctuation in the number density of very bright, i.e. $F_{500} \gtrsim 200$ mJy, lensed galaxies between the GAMA+NGP fields (13 detections) and the SGP field (only one detection). However, we have shown, also by means of numerical simulations, that these variations, although extreme, are still consistent with expectations based on Poisson statistics. Once we combine the samples from all the *H*-ATLAS fields, the derived number counts are consistent with those measured for the candidate lensed galaxies in HeLMS+HerS (Nayyeri et al. 2016).

This *H*-ATLAS catalogue of candidate lensed galaxies will provide valuable targets for follow-up observations aimed at studying with unprecedented detail the morphological and dynamical properties of DSFGs at $z \sim 2$, as recently demonstrated by the analysis of the high-resolution ALMA observations of SDP.81 (ALMA partnership 2015; Dye et al. 2015; Hatsukade et al. 2015; Rybak et al. 2015a,b; Swinbank et al. 2015; Tamura et al. 2015; Hezaveh et al. 2016), one of the first lensed galaxies discovered with *Herschel* (Negrello et al. 2010).

[6] 12 is the expectation value based on the observed number of lensed galaxies in the GAMA+NGP field rescaled to the 300 deg^2 area of the simulations.

ACKNOWLEDGEMENTS

Herschel is an ESA space observatory with science instruments provided by European-led Principal Investigator consortia and with important participation from NASA. We thank the anonymous referee for helpful suggestions and useful comments. This project has received funding from the European Union's Horizon 2020 research and innovation programme under the Marie Sklodowska-Curie grant agreement no. 707601. This work was supported by ASI/INAF Agreement 2014-024-R.0, by PRIN-INAF 2012 project 'Looking into the dust-obscured phase of galaxy formation through cosmic zoom lenses in the Herschel Astrophysical Large Area Survey'. JG-N acknowledges financial support from the Spanish MINECO for a 'Ramon y Cajal' fellowship (RYC-2013-13256) and the I+D 2015 project AYA2015-65887-P (MINECO/FEDER). LD, RJI and SJM acknowledge support from the European Research Council Advanced Investigator grant, COSMICISM. LD and SJM also acknowledge support from the European Research Council Consolidator grant, cosmicdust. SD acknowledges support by a STFC Ernest Rutherford Fellowship. CF acknowledges funding from CAPES (proc. 12203-1). JLW is supported by a European Union COFUND/Durham Junior Research Fellowship under EU grant agreement number 267209, and acknowledges additional support from STFC (ST/L00075X/1). CEP, CT, GV and LVEK are supported through an NWO-VICI grant (project number 639.043.308). LM is supported by the Science and Technology Facilities Council grant ST/J001597/1 and by a South African DST-NRF Fellowship for Early Career Researchers from the UK. Some of the observations reported in this paper were obtained with the Southern African Large Telescope (SALT) under proposal 2015-2-MLT-006. *Herschel* is an ESA space observatory with science instruments provided by European-led Principal Investigator consortia and with important participation from NASA. The *Herschel*-ATLAS is a project with *Herschel*, which is an ESA space observatory with science instruments provided by European-led Principal Investigator consortia and with important participation from NASA. The *H*-ATLAS website is http://www.h-atlas.org/. The Submillimeter Array is a joint project between the Smithsonian Astrophysical Observatory and the Academia Sinica Institute of Astronomy and Astrophysics and is funded by the Smithsonian Institution and the Academia Sinica. Support for CARMA construction was derived from the G. and B. Moore Foundation, the K. T. and E. L. Norris Foundation, the Associates of the California Institute of Technology, the states of California, Illinois, and Maryland, and the NSF. CARMA development and operations were supported by the NSF under a cooperative agreement, and by the CARMA partner universities. This research has made use of ALADIN and of the NASA/IPAC Extragalactic Database (NED) which is operated by the Jet Propulsion Laboratory, California Institute of Technology, under contract with the National Aeronautics and Space Administration.

REFERENCES

Abazajian K. et al., 2009, ApJS, 182, 543
ALMA partnership, 2015, ApJ, 808, 4
Amber S., 2015, PhD thesis, The Open University
Barnabè M., Czoske O., Koopmans L. V. E., Treu T., Bolton A. S., 2011, MNRAS, 415, 2215

Blain A. W., 1996, MNRAS, 283, 1340B
Bonnarel F. et al., 2000, A&AS, 143, 33
Bourne N. et al., 2016, MNRAS, 462, 1714
Bussmann S. et al., 2012, ApJ, 756, 134
Bussmann S. et al., 2013, ApJ, 779, 25
Bussmann S. et al., 2015, ApJ, 812, 43
Cai Z.-Y. et al., 2013, ApJ, 768, 21
Calanog J. A. et al., 2014, ApJ, 797, 138
Cañameras R. et al., 2015, A&A, 581, 105
Carlstrom J. E. et al., 2011, PASP, 123, 568
Chapin E. L. et al., 2011, MNRAS, 411, 505
Ciliegi P., Zamorani G., Hasinger G., Lehmann I., Szokoly G., Wilson G., 2003, A&A, 398, 901
Colless M. et al., 2001, MNRAS, 328, 1039
Conley A. et al., 2011, ApJ, 732, L35
Cox P. et al., 2011, ApJ, 740, 63
Dalal N., Kochanek C. S., 2002, ApJ, 572, 25
De Breuck C. et al., 2014, A&A, 565, 59
de Jong J. T. A. et al., 2015, A&A, 582, A62
Driver S. P. et al., 2009, Astron. Geophys., 50, 12
Driver S. P. et al., 2016, MNRAS, 455, 3911
Dye S. et al., 2014, MNRAS, 440, 2013
Dye S. et al., 2015, MNRAS, 452, 2258
Eales S., 2015, MNRAS, 446, 3224
Eales S. et al., 2010, PASP, 122, 499
Edge A., Sutherland W., Kuijken K., Driver S., McMahon R., Eales S., Emerson J. P., 2013, MNRAS, 409, 109
Frayer D. et al., 2011, ApJ, 726, L22
Fu H. et al., 2012, ApJ, 753, 134
Furlanetto C. et al., 2016, MNRAS, in press
Gehrels N., 1986, ApJ, 303, 336
George R. D. et al., 2013, MNRAS, 436, 99
Glenn J. et al., 2010, MNRAS, 409, 109
Gonzalez-Nuevo J. et al., 2010, A&A, 518, 38
Gonzalez-Nuevo J. et al., 2012, ApJ, 749, 65
Griffin M. J. et al., 2010, A&A, 518, L3
Grillo C., Lombardi M., Bertin G., 2008, A&A, 477, 397
Harrington K. C. et al., 2016, MNRAS, 458, 4383
Harris A. et al., 2012, ApJ, 752, 152
Hatsukade B., Tamura Y., Iono D., Matsuda Y., Hayashi M., Oguri M., 2015, PASJ, 67, 93
Hezaveh Y. D., Dalal N., Holder G., Kuhlen M., Marrone D., Murray N., Vieira J, 2013, ApJ, 767, 9
Hezaveh Y. D. et al., 2016, ApJ, 823, 37
Hodge J. A., Riechers D., Decarli R., Walter F., Carilli C. L., Daddi E., Dannerbauer H., 2015, ApJ, 798, L18
Hodge J. A. et al., 2016, ApJ, preprint (arXiv:1609.09649)
Ikarashi S. et al., 2015, ApJ, 810, 133
Inoue K. T., Minezaki T., Matsushita S., Chiba M., 2016, MNRAS, 457, 2936
Ivison R. et al., 2013, ApJ, 772, 137
Kormann R., Schneider P., Bartelmann M., 1994, A&A, 284, 285
Lapi A., Shankar F, . Mao J., Granato G., Silva L., De zotti G., Danese L., 2006, ApJ, 650, 42
Lapi A. et al., 2011, ApJ, 742, 24
Lapi A., Negrello M., González-Nuevo J., Cai Z.-Y., De Zotti G., Danese L., 2012, ApJ, 755, 46
Lawrence A. et al., 2007, MNRAS, 379, 1599
Lima M., Jain B., Devlin M., 2010, MNRAS, 406, 2352
Lindroos L. et al., 2016, MNRAS, 462, 1192
Lopez-Caniego M. et al., 2013, MNRAS, 430, 1566
Lupu R. et al., 2012, ApJ, 757, 135
Magnelli B. et al., 2012, A&A, 539, A155
Mao S., Schneider P., 1998, MNRAS, 295, 587
Messias H. et al., 2014, A&A, 568, 92
Metcalf R. B., Madau P., 2001, ApJ, 563, 9
More A., Cabanac R., More S., Alard C., Limousin M., Kneib J.-P., Gavazzi R., Motta V., 2012, ApJ, 749, 38
Nayyeri H. et al., 2016, ApJ, 823, 17
Negrello M., Perrotta F., González-Nuevo J., Silva L., de Zotti G., Granato G. L., Baccigalupi C., Danese L., 2007, MNRAS, 377, 1557
Negrello M. et al., 2010, Science, 330, 800
Negrello M. et al., 2014, MNRAS, 440, 1999
Oliver S. J. et al., 2012, MNRAS, 424, 1614
Omont A. et al., 2011, A&A, 530, L3
Omont A. et al., 2013, A&A, 551, A115
Peacock J. A., 1982, MNRAS, 199, 987
Pearson E. A. et al., 2013, MNRAS, 435, 2753
Perrotta F., Baccigalupi C., Bartelmann M., De Zotti G., Granato G. L., 2002, MNRAS, 329, 445
Perrotta F., Magliocchetti M., Baccigalupi C., Bartelmann M., De Zotti G., Granato G. L., Silva L., Danese L., 2003, MNRAS, 338, 623
Pilbratt G. et al., 2010, A&A, 518, 1
Planck Collaboration XIII, 2016, A&A, 594, A13
Planck Collaboration XXVII, 2015, A&A, 582, A30
Poglitsch A. et al., 2010, A&A, 518, L2
Prada F., Klypin A. A., Cuesta A. J., Betancort-Rijo J. E., Primack J., 2012, MNRAS, 423, 3018
Richter G. A., 1975, Astron. Nachr., 296, 65
Riechers D. et al., 2013, Nature, 496, 329
Riechers D. et al., 2014, ApJ, 796, 84
Rybak M., McKean J. P., Vegetti S., Andreani P., White S. D. M., 2015a, MNRAS, 451, L40
Rybak M., Vegetti S., McKean J. P., Andreani P., White S. D. M., 2015b, MNRAS, 453, 26
Serjeant S., 2016, Proc. Sci., Synergies between SALT and Herschel, Euclid and the SKA: Strong Gravitational Lensing and Galaxy Evolution. SISSA, Treiste
Sheth R., Tormen G., 1999, MNRAS, 308, 119
Simpson J. M. et al., 2014, ApJ, 788, 125
Simpson J. M. et al., 2015, ApJ, 799, 81
Spilker J. S. et al., 2016, ApJ, 826, 112
Sutherland W., Saunders W., 1992, MNRAS, 259, 413
Stanford et al., 2014, ApJS, 213, 25
Swinbank M. et al., 2010, Nature, 464, 733
Swinbank M. et al., 2015, ApJ, 806, 17
Tamura Y., Oguri M., Iono D., Hatsukade B., Matsuda Y., Hayashi M., 2015, PASJ, 67, 72
Tucci M., Toffolatti L., de Zotti G., Martínez-González E., 2011, A&A, 533, 57
Valiante E. et al., 2016, MNRAS, 462, 3146
Valtchanov et al., 2011, MNRAS, 415, 3473
Vegetti S., Lagattuta D. J., McKean J. P., Auger M. W., Fassnacht C. D., Koopmans L. V. E., 2012, Nature, 481, 341
Vieira J. et al., 2013, Nature, 495, 344
Viero M. P. et al., 2014, ApJS, 210, 22
Wardlow J. et al., 2013, ApJ, 762, 59
Weiß A. et al., 2013, ApJ, 767, 88
Yang C. et al., 2016, A&A, 595, A80

APPENDIX A: POSTAGE STAMPS OF CANDIDATE LENSED GALXIES

We show here optical to near-IR postage stamp images of the candidate lesed galaxies with $F_{500} \geq 100$ mJy identified in the *H*-ATLAS fields, and with lensing rank B or C.

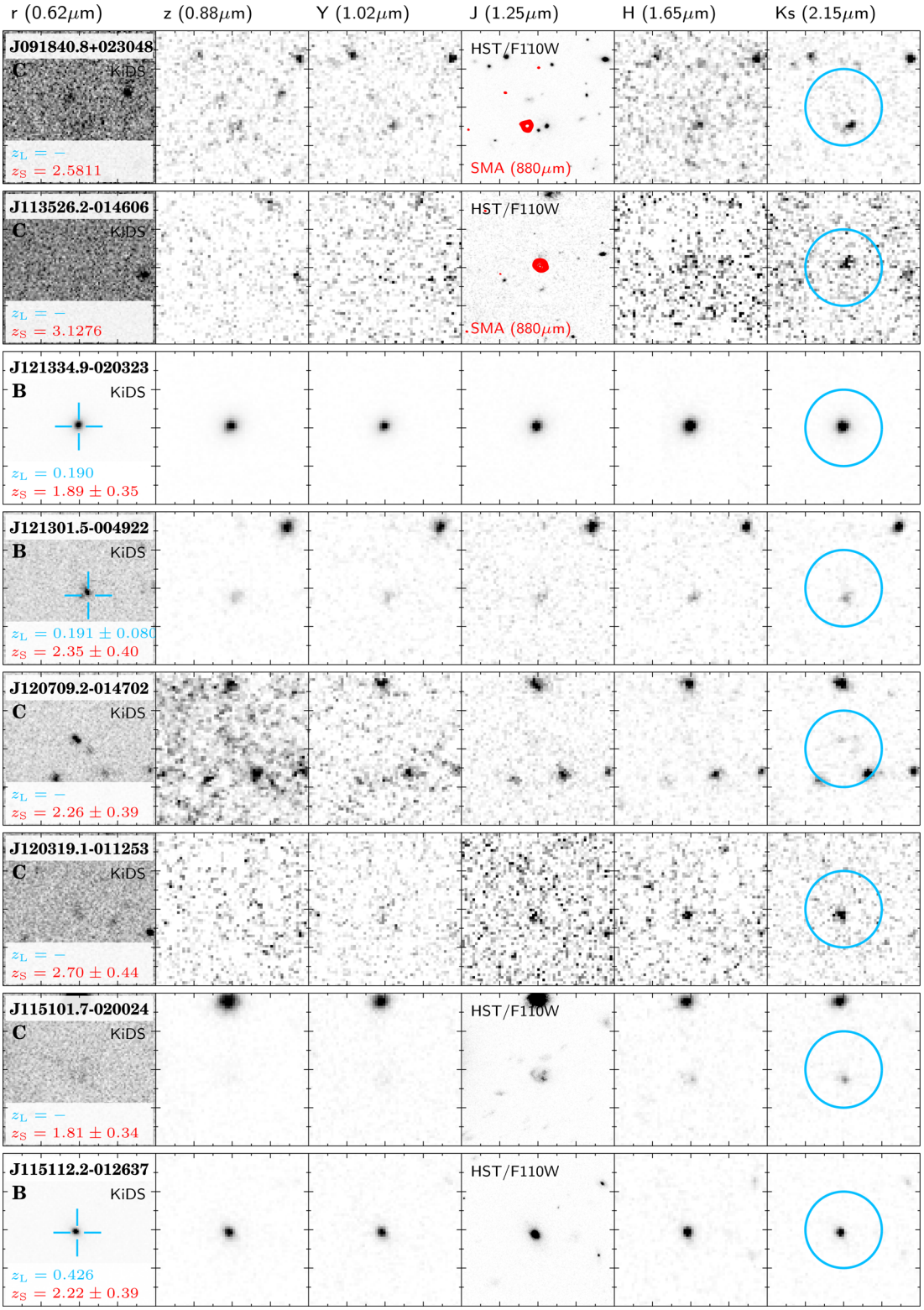

Figure A1. 20 arcsec × 20 arcsec postage stamps of candidate lensed galaxies with $F_{500} \geq 100$ mJy and with lensing rank B or C extracted from the *H*-ATLAS equatorial fields, centred at the position of the *Herschel*/SPIRE detection. Imaging data are from KiDS (r band) and VIKING (Z, Y, J, H, K_s bands). The VIKING J-band image is replaced by the *HST*/*F*110*W* image when *HST* data are available. For each source, the optical and the sub-mm redshifts are shown at the bottom of the r-band stamp, while, in the same stamp, the lensing rank is shown on the top-left corner. The uncertainty on redshift is reported only when the value of z is photometrically derived. Where a reliable ($R > 0.8$) optical counterpart is found (see Table 4), its position is marked by a cross in the r-band images. A circle of 5 arcsec in radius, centred at the position of the SPIRE detection, is shown in the K_s images. Where available, SMA contours at 880 μm are shown in red.

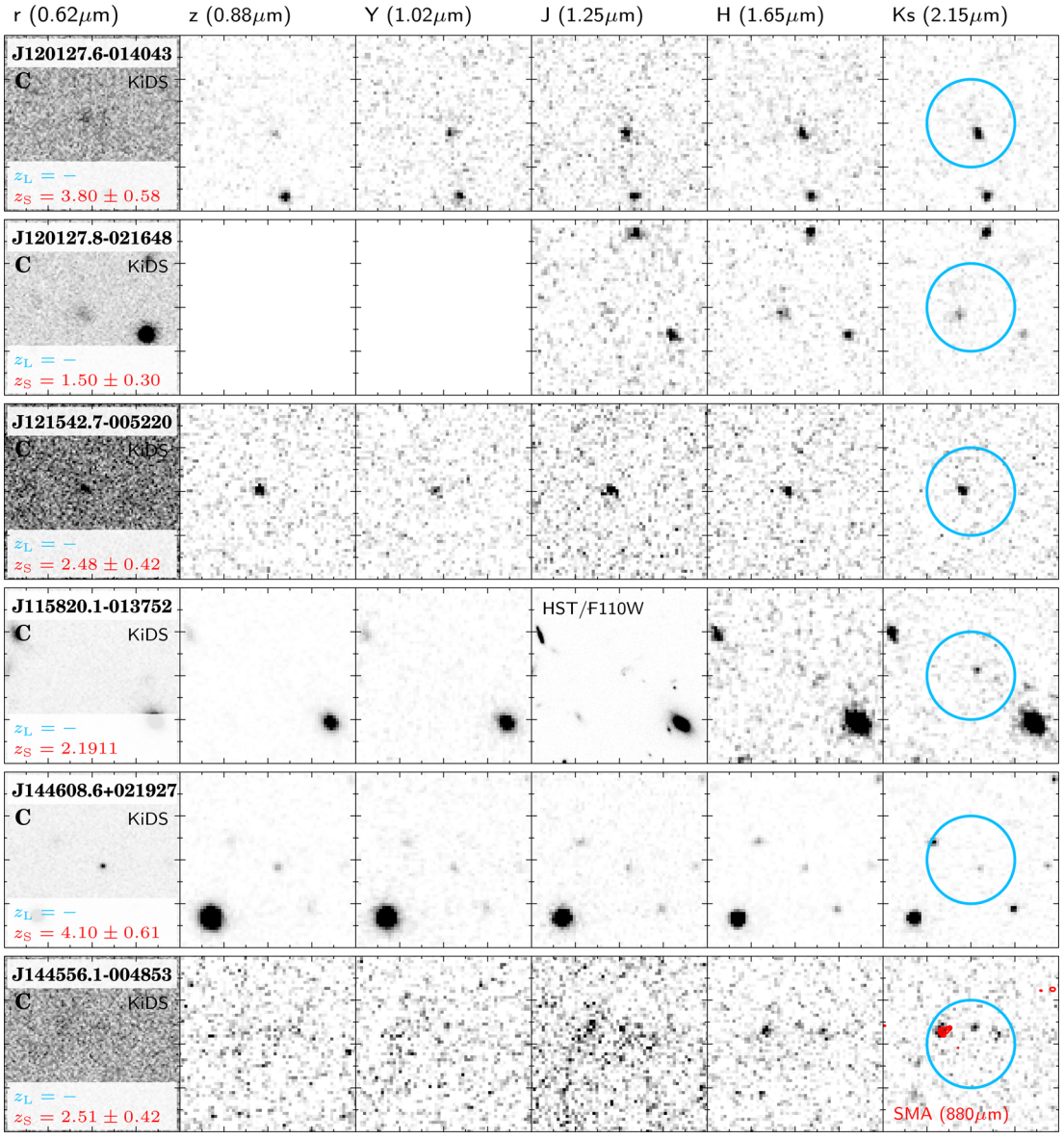

Figure A1 – *continued*

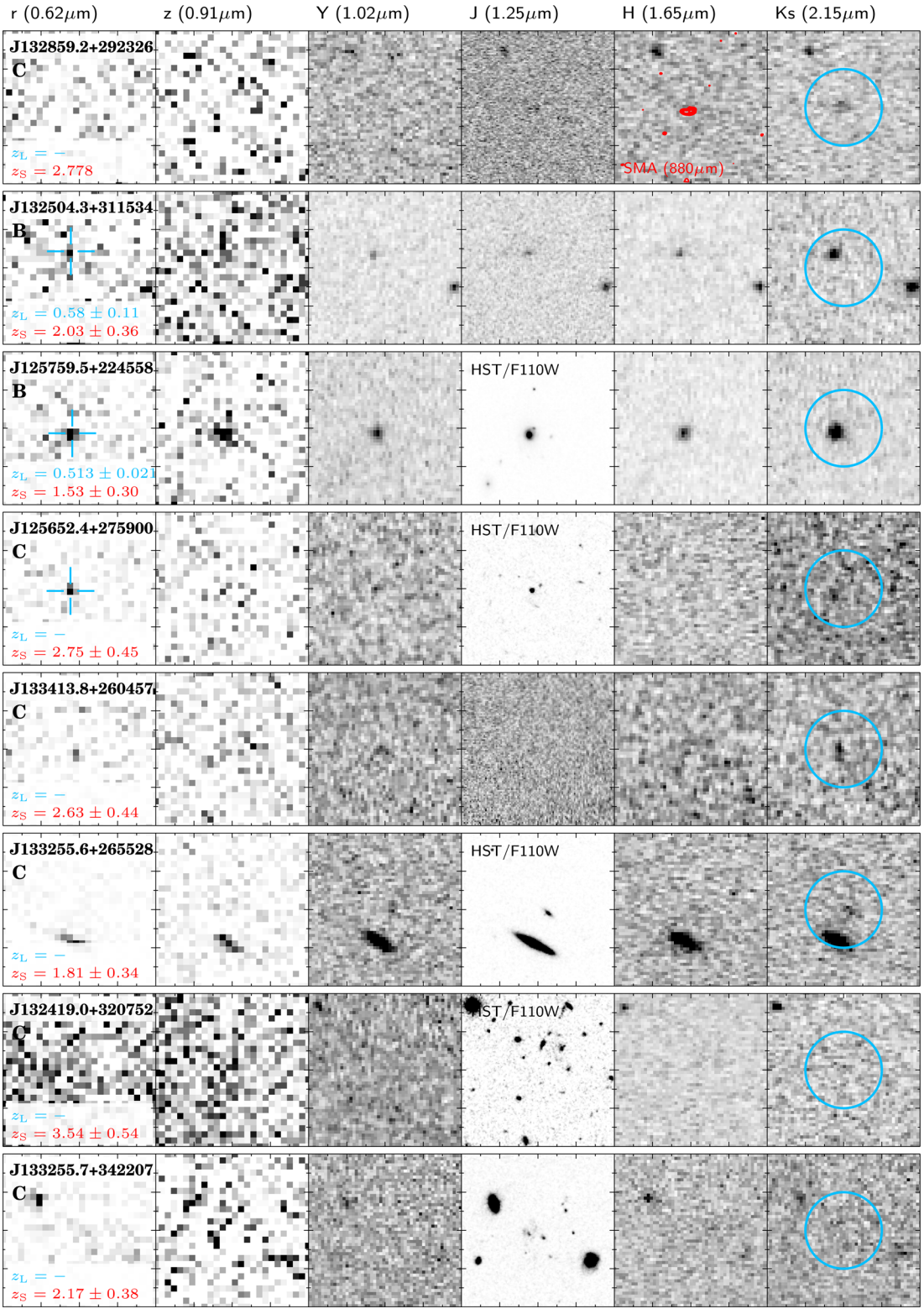

Figure A2. 20 arcsec × 20 arcsec postage stamps of candidate lensed galaxies with $F_{500} \geq 100$ mJy and with lensing rank B or C extracted from the *H*-ATLAS/NGP field, centred at the position of the *Herschel*/SPIRE detection. Imaging data are from SDSS (*r* and *z* bands) and UKIDSS-LAS (*Y*, *J*, *H*, K_s bands). The UKIDSS *J*-band image is replaced by the *HST*/*F*110*W* image when *HST* data are available. For each source, the optical and the sub-mm redshifts are shown at the bottom of the *r*-band stamp, while, in the same stamp, the lensing rank is shown on the top-left corner. The uncertainty on redshift is reported only when the value of *z* is photometrically derived. Where a reliable optical ($R > 0.8$) counterpart is found (see Table 4), its position is marked by a cross in the *r*-band images. A circle that is 5 arcsec in radius, centred at the position of the SPIRE detection, is shown in the K_s images. Where available, SMA contours at 880 μm are shown in red.

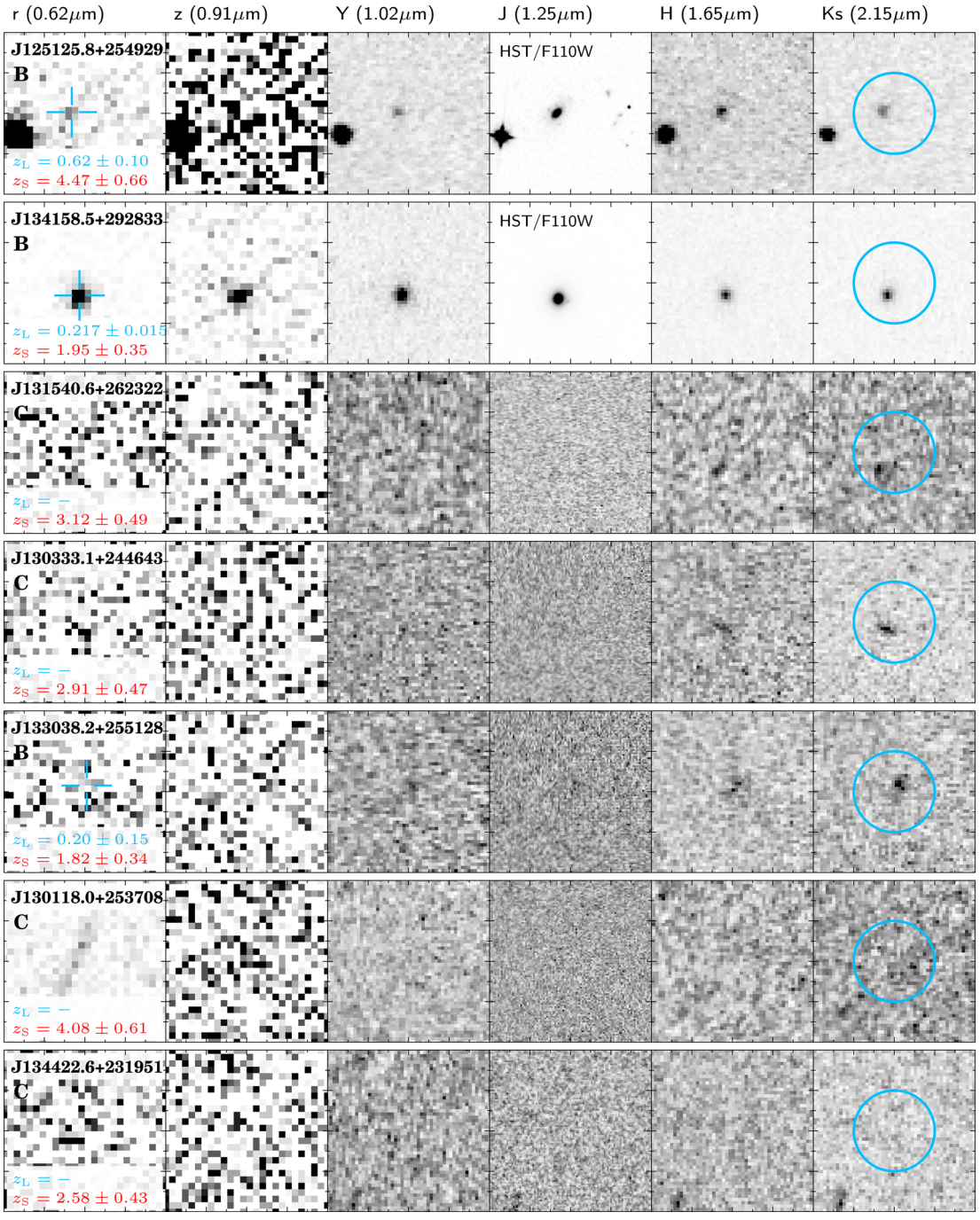

Figure A2 – *continued*

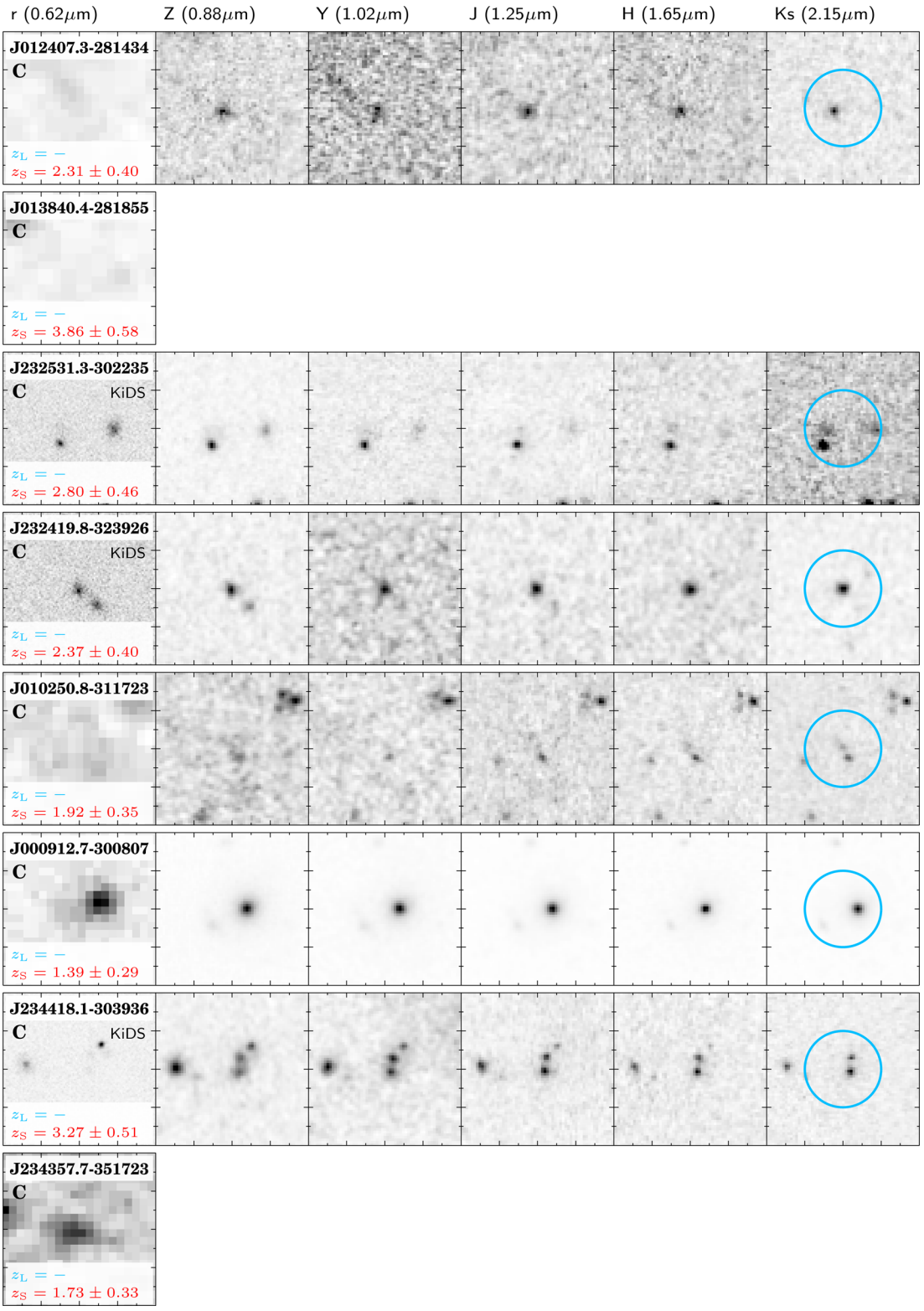

Figure A3. 20 arcsec × 20 arcsec postage stamps of candidate lensed galaxies with $F_{500} \geq 100$ mJy and with lensing rank B or C extracted from the *H*-ATLAS/SGP field, centred at the position of the *Herschel*/SPIRE detection. Imaging data are from the Digitalized Sky Survey (DSS; *r* band), or KiDS (*r* band) where available, and VIKING (*Z*, *Y*, *J*, *H*, K_s bands). For each source, the optical and the sub-mm redshifts are shown at the bottom of the *r*-band stamp, while, in the same stamp, the lensing rank is shown on the top-left corner. The uncertainty on redshift is reported only when the value of *z* is photometrically derived. A circle that is 5 arcsec in radius, centred at the position of the SPIRE detection, is shown in the K_s images.

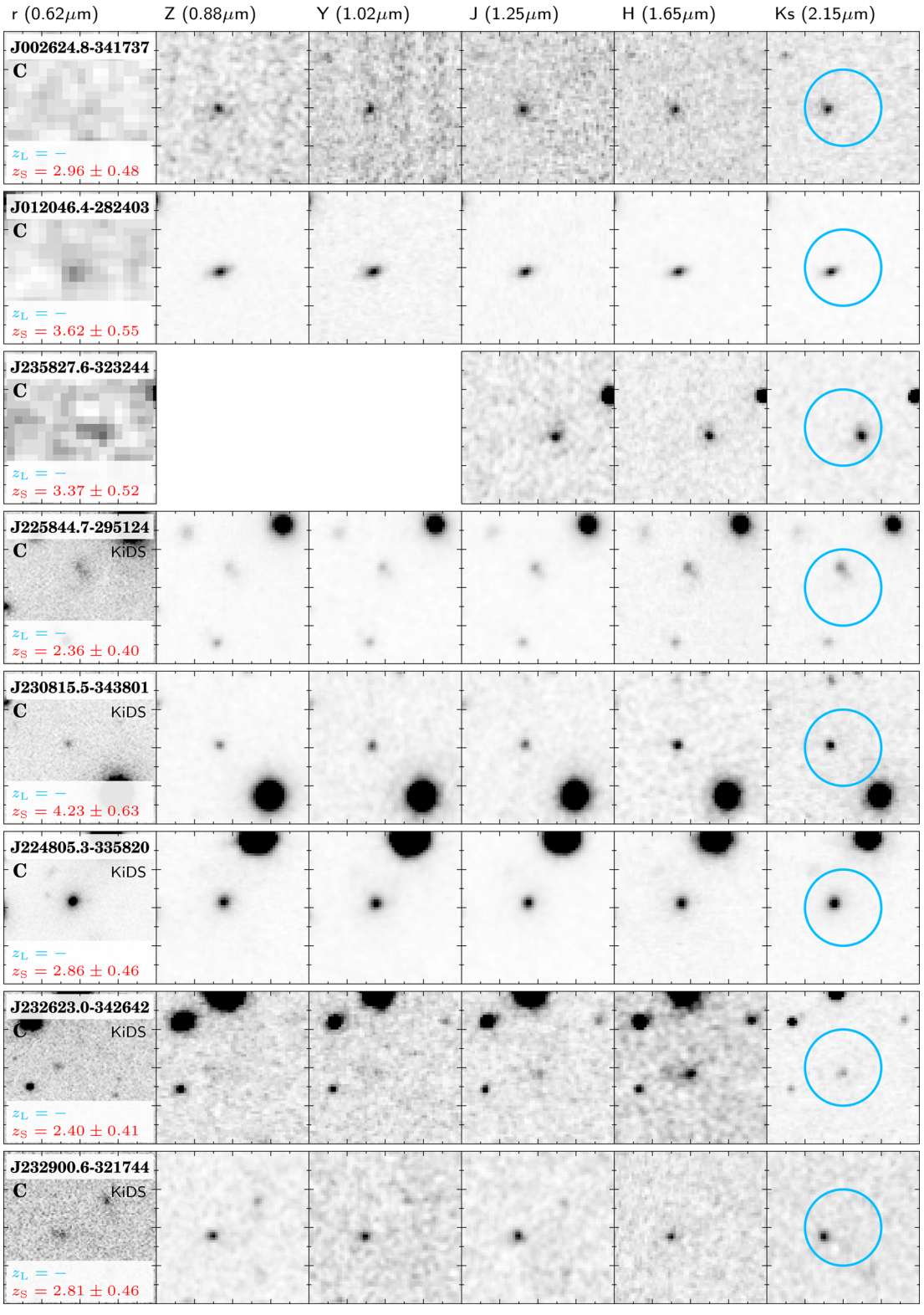

Figure A3 – *continued*

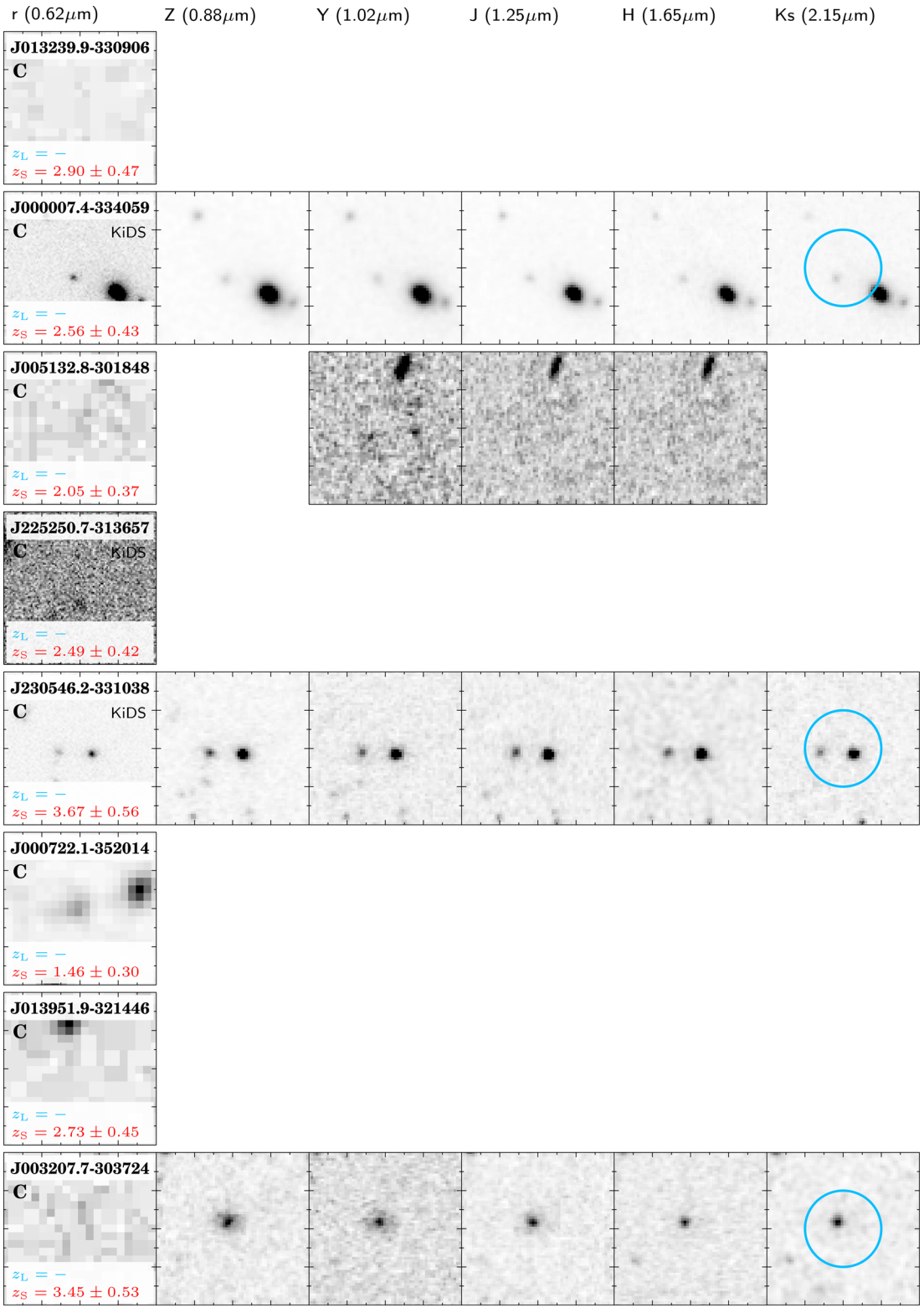

Figure A3 – *continued*

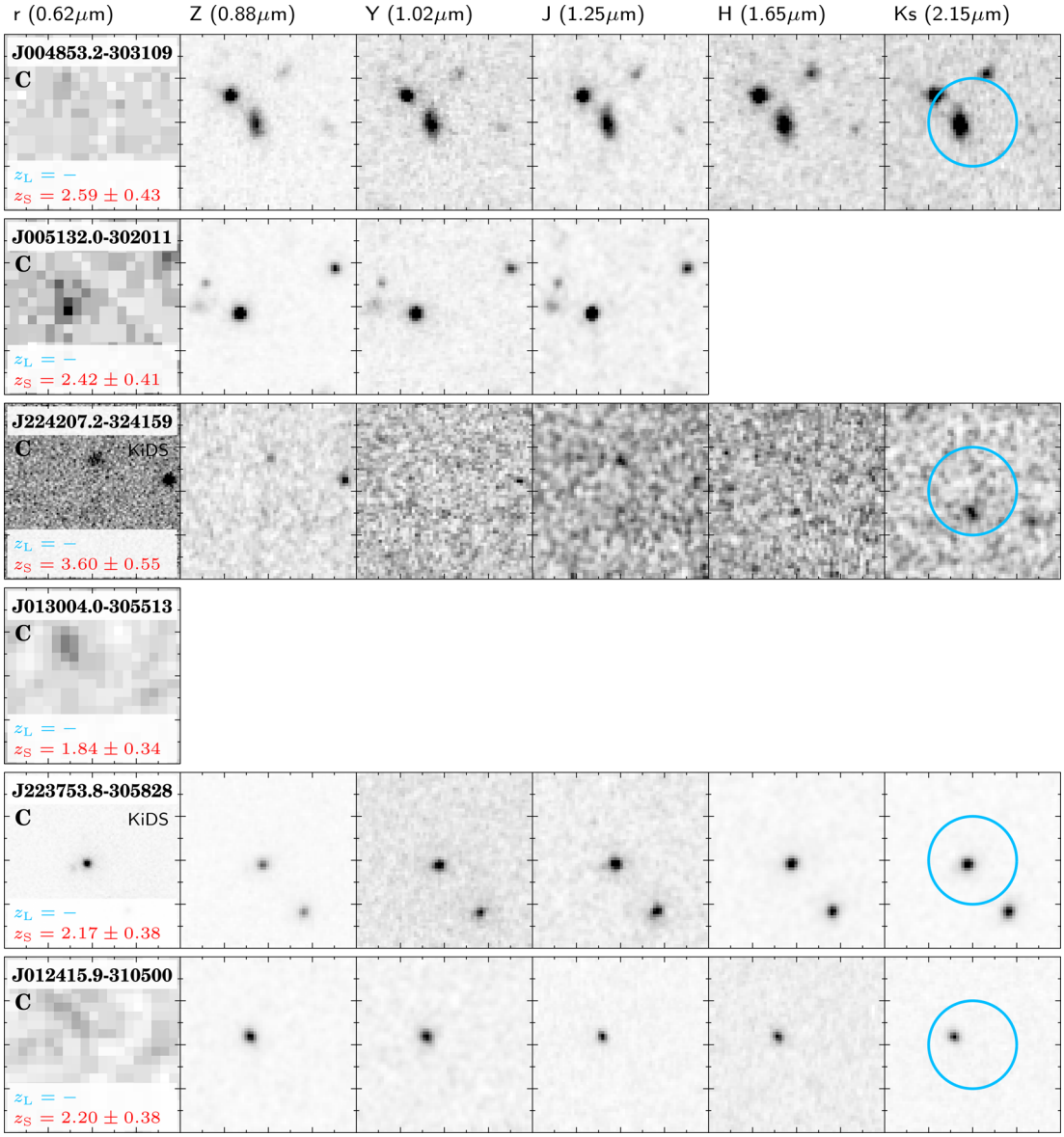

Figure A3 – *continued*

[1]*School of Physics and Astronomy, Cardiff University, The Parade, Cardiff CF24 3AA, UK*
[2]*Department of Physical Sciences, The Open University, Walton Hall, Milton Keynes MK7 6AA, UK*
[3]*CAS Key Laboratory for Research in Galaxies and Cosmology, Department of Astronomy, University of Science and Technology of China, Hefei, Anhui 230026, China*
[4]*Dipartimento di Fisica, Universita Tor Vergata, Via Ricerca Scientifica 1, I-00133 Roma, Italy*
[5]*SISSA, Via Bonomea 265, I-34136 Trieste, Italy*
[6]*Departamento de Física, Universidad de Oviedo, C. Calvo Sotelo s/n, E-33007 Oviedo, Spain*
[7]*INAF, Osservatorio Astronomico di Padova, Vicolo Osservatorio 5, I-35122 Padova, Italy*
[8]*School of Physics and Astronomy, University of Nottingham, University Park, Nottingham NG7 2RD, UK*
[9]*CAPES Foundation, Ministry of Education of Brazil, Brasília/DF 70040-020, Brazil*
[10]*Institute for Astronomy, University of Edinburgh, Royal Observatory, Blackford Hill, Edinburgh EH9 3HJ, UK*
[11]*Department of Astronomy, Space Science Building, Cornell University, Ithaca, NY 14853, USA*
[12]*Department of Physics & Astronomy, University of California, Irvine, CA 92697, USA*
[13]*Dipartimento di Fisica, Università di Napoli 'Federico II', Via Cinthia, I-80126 Napoli, Italy*
[14]*Instituto de Astrofísica de Canarias (IAC), E-38205 La Laguna, Tenerife, Spain*
[15]*Universidad de La Laguna, Dpto. Astrofisica, E-38206 La Laguna, Tenerife, Spain*
[16]*Department of Physics & Astronomy, University of Iowa, Iowa City, IA 52242, USA*
[17]*Blackett Laboratory, Imperial College London, Prince Consort Road, London SW7 2AZ, UK*
[18]*Harvard–Smithsonian Center for Astrophysics, 60 Garden Street, Cambridge, MA 02138, USA*
[19]*Kapteyn Astronomical Institute, University of Groningen, PO Box 800, NL-9700 AV Groningen, the Netherlands*
[20]*INAF – Osservatorio Astronomico di Capodimonte, Via Moiariello 16, I-80131 Napoli, Italy*

[21] *UPMC Univ. Paris 06, UMR7095, Institut d'Astrophysique de Paris, F-75014 Paris, France*
[22] *CNRS, UMR7095, Institut d'Astrophysique de Paris, F-75014 Paris, France*
[23] *Centre for Extragalactic Astronomy, Department of Physics, Durham University, South Road, Durham DH1 3LE, UK*
[24] *Sterrenkundig Observatorium, Universiteit Gent, Krijgslaan 281 S9, B-9000 Gent, Belgium*
[25] *Department of Physics and Astronomy, Rutgers, the State University of New Jersey, 136 Frelinghuysen Road, Piscataway, NJ 08854-8019, USA*
[26] *South African Astronomical Observatory, PO Box 9, Observatory, 7935 Cape Town, South Africa*
[27] *European Southern Observatory, Karl-Schwarzschild-Strasse 2, D-85748 Garching, Germany*
[28] *Department of Physics and Astronomy, University of the Western Cape, Robert Sobukwe Road, 7535 Bellville, Cape Town, South Africa*
[29] *INAF – Istituto di Radioastronomia, via Gobetti 101, I-40129 Bologna, Italy*
[30] *Leiden Observatory, Leiden University, PO Box 9513, NL-2300 RA Leiden, the Netherlands*

This paper has been typeset from a TEX/LATEX file prepared by the author.